https://doi.org/10.5194/egusphere-2026-4492
Preprint. Discussion started: 31 July 2026

The TRISHNA Mission: A New Era of High-Resolution Thermal Infrared Earth Observation for Land Surface Monitoring

Philippe Gamet[1,2], Bimal K. Bhattacharya[3], Jean-Louis Roujean[2], Gilles Boulet[2,11], Corinne Salcedo[1], Albert Olioso[6], Kanishka Mallick[2], Marie Weiss[6], Emmanuelle Sarrazin[1,2], Emmanuelle Autret[8], Laure Roupioz[7], José Antonio Sobrino[5], Olivier Merlin[2], Ghislain Picard[10], Thomas H.G. Vidal[9], Mark Irvine[6], Rahul Nigam[3], Mehul Pandya[3], Simon Gascoin[2], Sébastien Marcq[1], Manoj K. Mishra[3], Emilie Delogu[1], Vincent Rivalland[2], Jordi Etchanchu[13], Jean-Louis Raynaud[1], Meenakshi Sarkar[3], Rishi K. Gangwar[3], Sushil K. Singh[3], Renaud Binet[1], Sara Arioli[14], Hervé Yesou[14], Isabelle Dadou[15], Alexei Kouraev[15], Julien Michel[1,2], Benoit Coudert[2], Samuel Mwangi[2], Nesrine Farhani[13], Ayan Das[3], Stéphane Saux-Picart[16], Thierry Tormos[17], Jean-François Piollé[8], Charles Verpoorter[20], Auline Rodler[18], Jonathan Leon Tavares[22], Jennifer Adams[19], Anand S. Sahadevan[3], Besavaraju Santhi Sree[4], Manikumar Vedantam[4], Dheeraj Adlakha[3], Laurence Buffet[1], Kathrin Naegeli[21], Itziar Barat[12], Jérôme Demarty[13], Olivier Hagolle[1,2], Philippe Maisongrande[1]

[1]CNES, Toulouse, 31400, France
[2]Centre d'Etudes Spatiales de la Biosphère (CESBIO), Toulouse, 31400, France
[3]Space Applications Center, Indian Space Research Organization, Ahmedabad, 380015, India
[4]National Remote Sensing Centre (NRSC), Hyderabad, 500037, India
[5]University of Valencia, Paterna, 46980, Spain
[6]URFM, INRAE, Avignon, 84000, France
[7]ONERA/DOTA, Université de Toulouse, F-31055 Toulouse, France
[8]Laboratoire d'Océanographie Physique et Spatiale (LOPS), IFREMER, Plouzané, 29280, France
[9]ACRI-ST, Toulouse, 31000, France
[10]Institut des Géosciences de l'Environnement, Unversity of Grenoble, Saint Martin d'Hères, 38400, France
[11]Indo-French Cell for Water Science, ICWaR, Indian Institute of Science, Bangalore, 560012, India
[12]ESTEC, European Space Agency, Noordwijk, 2201, The Netherlands
[13]HydroSciences Montpellier (HSM), Montpellier, 34090, France
[14]SERTIT, University of Strasbourg, Illkirch-Graffenstaden, 67218, France
[15]Laboratoire d'Etudes en Géophysique et Océanographie Spatiales (LEGOS), Toulouse, 31400, France
[16]Meteofrance Centre de Météorologie Spatiale, Lannion, 22307, France
[17]Office Français de la Biodiversité (OFB), Aix-en-Provence, 13592, France
[18]CEREMA, Nantes, 44200, France
[19]CMCC Foundation, Euro-Mediterranean Centre on Climate Change, Viterbo, 01100, Italy
[20]University of Littoral Côte d'Opale, Laboratoire d'Océanologie et de Géosciences (LOG), Wimereux, 62930, France
[21]University of Zürich, Zürich, 8057, Switzerland
[22]Flemish Institute for Technological Research (VITO), 2400, Belgium

Correspondence to: Philippe Gamet (Philippe.Gamet@cnes.fr), Bimal K. Bhattacharya (bkbhattacharya@sac.isro.gov.in)

Abstract. Thermal infrared (TIR) satellite remote sensing is essential for monitoring land surface temperature (LST) and surface energy fluxes, supporting applications in hydrology, agriculture, climate, and urban climate. Existing TIR missions—such as LANDSAT, ASTER, ECOSTRESS, and Sentinel-3 SLSTR—offer complementary capabilities but remain constrained by trade-offs between spatial resolution, revisit frequency, and radiometric accuracy, limiting their ability to capture rapidly evolving surface processes at field to regional scales.

The TRISHNA (Thermal Infrared Satellite for High-Resolution Natural Resource Assessment) mission, expected in 2027, addresses this gap by providing 60 m TIR imagery over a ~1000 km swath with sub-weekly revisit, enabling systematic monitoring of surface energy processes in natural and managed ecosystems. Its integrated design —including orbit configuration, spectral channels (VNIR, SWIR, TIR), viewing geometry, and calibration strategy— supports accurate retrievals of evapotranspiration, vegetation water stress, and surface temperature dynamics. Synergies with upcoming missions

https://doi.org/10.5194/egusphere-2026-4492
Preprint. Discussion started: 31 July 2026

such as ESA's Land Surface Temperature Mission (LSTM) and NASA's EAGLE mission (Explorer for Artemis Geology Lunar and Earth) will enhance temporal coverage, cross-calibration, and long-term data continuity.

1 Introduction

Thermal infrared (TIR) satellite remote sensing is a fundamental component of Earth observation, enabling the monitoring of land surface temperature (LST) and surface energy exchanges across a wide range of spatial and temporal scales (Li et al., 2013). The spatial and temporal variability of the LST reflects the combined effects of surface properties, vegetation cover, soil moisture, and atmospheric forcing, making it a physically rich indicator of surface processes (Anderson et al., 2008).
Satellite-derived LST has become indispensable for numerous scientific and operational applications. In hydrology and agronomy, LST is a central input for evapotranspiration estimation (Kalma et al., 2008) and vegetation water stress monitoring (Boulet et al., 2007), directly supporting irrigation management and food security assessments (Bastiaanssen et al., 1998, Courault et al. 2005). In climate and environmental studies, LST contributes to the analysis of surface warming trends, heat extremes, and land–atmosphere feedbacks, while in urban environments it enables the characterization of thermal heterogeneity and urban heat island intensity (Voogt and Oke, 2003). Moreover, LST is a key variable for monitoring environmental phenomena: pollutant degradation (Louchart and Voltz, 2007), pathogen dissemination (Sobrino et al., 2016). These applications require observations with high spatial resolution, frequent revisit, and robust radiometric accuracy.
Existing spaceborne thermal infrared missions provide complementary but incomplete coverage of user needs (Cawse-Nicholson et al., 2026). Indeed, from an observational standpoint, existing thermal infrared missions span a wide but fragmented range of spatial and temporal scales. The LANDSAT series provides TIR observations at native spatial resolutions of 100 m (resampled to 30 m), with a swath width of ~185 km and a nominal revisit period of 16 days per satellite, which limits its ability to monitor rapidly evolving surface thermal and hydrological processes (Markham et al., 2012; Barsi et al., 2010). ASTER (Abrams et al., 2002) provides global land surface multispectral products derived from 14 spectral bands spanning VNIR, SWIR, and TIR, with spatial resolutions of 15 m (VNIR), 30 m (SWIR), and 90 m (TIR), again with a revisit time of ~16 days. The TIR instrument was decommissioned in 2026. ECOSTRESS (Fisher et al., 2020) provides variable local overpass times from the International Space Station (ISS), with spatial resolutions of approximately 70 m. However, its coverage is geographically irregular, as its revisit depends on latitude and ISS orbit dynamics, and its swath width remains limited (384 km) relative to global mapping requirements. There are also several missions at coarser resolution such as Sentinel-3 SLSTR (Pérez-Planells et al., 2021) providing highly stable, radiometrically accurate TIR measurements with near-global coverage, wide swath (~1400 km), and revisit times of one to two days, but at spatial resolutions of about 1 km, which are insufficient for field-scale agricultural, hydrological, and urban applications. There are also privately owned high-resolution satellites with TIR capability, which are designed to acquire data on demand.
The French scientific community has identified the gap in TIR observation capability three decades ago and submitted various proposals to CNES (Centre National d'Etudes Spatiales) and ESA (European Space Agency). IRSUTE (InfraRed minisatellite for Surface Temperature and emissivity estimation for land sUrface heat flux Estimation, Seguin et al., 1999) was a TIR satellite mission concept developed in the 2000s, primarily within the French scientific community with strong involvement from CNES and academic laboratories. Although IRSUTE was not selected for flight, its scientific legacy gave birth to the following studies: MISTIGRI, a study for a microsatellite in the thermal infrared conducted from 2009 to 2012 by CNES in cooperation with Spain (Lagouarde et al., 2013) and TIREX (Sobrino et al., 2010), a proposal made at ESA to the Earth Explorer 8 call for Opportunity Missions. These projects proposed to combine high spatial resolution (~50 m), with high revisit capabilities of 1 or 2 days. Due to constraints of the microbolometer technology, these missions were designed for demonstration, i.e., targeting only a few selected regions on the planet. None of them progressed beyond the concept phase.

https://doi.org/10.5194/egusphere-2026-4492
Preprint. Discussion started: 31 July 2026

Recent technological progress across detector physics, instrument design, calibration systems, and data processing infrastructure has opened new opportunities for TIR Earth observation. Historically, high spatial resolution TIR imaging from space was limited by the need for large, cryogenically cooled detectors and complex radiometric calibration systems, which increased mass, cost, and mission risk. Advances in large-format infrared focal plane arrays, improved cryocooler efficiency, and onboard calibration techniques now make it feasible to achieve high radiometric sensitivity and stability in moderate-sized platforms suited for systematic Earth observation (Han and Zhang, 2022).

These technology enablers are directly reflected in a new generation of multispectral thermal infrared instruments, which was pioneered by the Prototype HyspIRI Thermal Infrared Radiometer (Lee et al., 2015). The THIRSTY (Thermal InfraRed Imaging Satellite for sTudY) mission was a joint CNES–JPL mission concept developed in the late 2010s based for the first time on this compact, cost-effective payload, consistent with medium- to small-class mission constraints (Crebassol et al., 2014). The mission itself was not pursued, as the instrument was ultimately selected for the ECOSTRESS mission, which became operational aboard the International Space Station in 2018. However, ECOSTRESS is not suitable for consistent large-scale monitoring because of its irregular revisit time, non-systematic acquisition, and lack of global coverage due to its position on the ISS.

TRISHNA (Thermal Infrared Satellite for High-Resolution Natural Resource Assessment, CNES/ISRO), expected to be launched in 2027, is designed to fill the observational gap between the existing systems by combining high spatial resolution thermal infrared imaging (less than 100 m) with a wide swath (~1000 km) and a revisit frequency of a few days at mid-latitudes. With this configuration, systematic, repeatable monitoring of land surface temperature and water stress is possible at spatial scales compatible with agricultural plots, irrigation districts, and heterogeneous landscapes, while maintaining temporal sampling adequate for capturing surface energy balance dynamics. As such, TRISHNA complements LANDSAT's spatial detail, ECOSTRESS's diurnal sensitivity, and Sentinel-3's global continuity, while uniquely addressing the requirements of operational water resource management and ecosystem monitoring.

However, it became clear that complimentarity of VNIR and SWIR observations is essential to achieve full potential of science and applications from TIR observations, as will be discussed in the following sections. ISRO has the legacy of conceptualizing and realizing wideswath four-band VNIR-SWIR Advanced Wide-Field Sensor (AWiFS) in Resourcesat series (1, 2, 2A), capable of observing land surface for natural resource monitoring at 56m spatial resolution with 5-day revisit period (Navalgund et al., 2007). The combination of CNES's four-band TIR payload and ISRO's seven-band VSWIR payload makes TRISHNA a unique global mission and the first of its kind.

The Land Surface Temperature Monitoring mission (LSTM), an ESA Copernicus expansion mission planned for the end of the decade, targets ~50 m thermal infrared resolution with a revisit period of 2 days (Koetz et al., 2018). The Surface Biology and Geology (SBG) mission, led by NASA in collaboration with the Italian Space Agency (ASI) and recently renamed EAGLE (Explorer for Artemis Geology Lunar and Earth), is designed to deliver high-resolution TIR imaging as part of its synergistic thermal, spectral, and SWIR payload suite, supporting global mapping of surface properties with plot-scale thermal detail (Stavros et al., 2023). The near-concurrent launch schedule (late-2020s / early-2030s timeframe) between TRISHNA, LSTM, and EAGLE-TIR promise enhanced temporal sampling and continuity in high-resolution land surface temperature products, supporting integrated studies of evapotranspiration, water stress, and surface energy dynamics at scales required for climate adaptation and resource management.

The data policy of the TRISHNA mission is aligned with the principles of the Copernicus program, under which data and information are made available "on a free, full and open basis" to all users worldwide upto certain spatial resolution, as established by the European Commission (Commission Delegated Regulation (EU) No 1159/2013) and and the Indian Space Policy (https://www.isro.gov.in/media_isro/pdf/IndianSpacePolicy2023.pdf). Adopting such a free, full and open access

https://doi.org/10.5194/egusphere-2026-4492
Preprint. Discussion started: 31 July 2026

approach for TRISHNA data aims to maximize their scientific and societal impact and to strengthen synergies with complementary missions.

The TRISHNA mission concept was introduced in Lagouarde et al., 2019, which provided a first comprehensive overview of the mission objectives and design. However, since this early definition phase, the mission has undergone significant maturation, including refinements in instrument characteristics, orbit configuration, product definition, calibration strategy, and ground segment architecture. An updated and more detailed description of the TRISHNA scientific rationale, mission design and system architecture is therefore proposed in this article, in order to reflect its current status and to provide the scientific community with an accurate and consolidated reference.

The mission design is primarily driven by the need to monitor ecosystem stress and water use, as well as coastal and inland waters, while also supporting applications such as urban microclimate characterization, cryospheric processes, and solid Earth studies. The design drivers place stringent requirements on spatial resolution, revisit frequency, spectral coverage, radiometric accuracy, and geometric performance, which are addressed through an integrated mission design approach.

Subsequent sections detail the mission design, including orbit selection, local observation time, viewing geometry, and spectral configuration, with particular emphasis on the definition of the thermal channels, and on the need for simultaneous VNIR, SWIR, and TIR acquisitions. The system and product architecture are then described, covering the flight and ground segments, processing chains, and data product levels. The article further outlines the calibration and validation strategy essential to ensuring data quality and long-term consistency, and discusses synergies with future and complementary missions. Together, these elements demonstrate how the proposed mission concept can deliver robust, interoperable data products that both complement and extend beyond current and planned capabilities for Earth system science and operational applications.

2 Science and applications

2.1 Ecosystem stress and water use

Evapotranspiration (ET) is an Essential Climate Variable (ECV, Bojinski et al., 2014), and a core component of the terrestrial hydrological cycle, representing the main pathway of water transfer from land to atmosphere (Bastiaanssen et al., 1998; Courault et al., 2005; Kalma et al., 2008). It is a key variable for irrigation management, water resources planning, and ecosystem studies (Allen et al., 2007; Anderson et al., 2012). As an integrative indicator of plant water uptake and regulation, ET reflects vegetation water constraints and is closely linked to canopy conductance, soil moisture, and vegetation stress (Moran et al., 1994; Berni et al., 2009; Boulet et al., 2007). ET is also a key variable in hydrology as it governs soil moisture depletion in surface and root zones, thereby soil water availability to plants, influencing infiltration, runoff, recharge, and catchment-scale water balance (Kustas and Norman, 1999; Crow et al., 2008; Su, 2002; Schuurmans et al., 2003, Ollivier et al., 2021).

Near-real-time ET is essential for irrigation scheduling and short-term stress detection (Anderson et al., 2012; Mu et al., 2013), whereas longer-term water accounting objectives can tolerate lower accuracy and latency (Jiang and Islam, 1999; Van der Kwast et al., 2009). Detecting temporal variability and trends in ET enable identification of emerging water stress, drought, and ecosystem vulnerability (Carlson, 2007; Anderson et al., 2007; Galleguillos et al., 2011), supporting adaptive irrigation, water footprinting, micro-watershed management, and early warning under climate variability and change (FAO, 2009; IPCC, 2014).

TRISHNA is primarily designed to address these challenges by providing routine, high-resolution global observations of land surface radiative temperature, enabling robust ET and vegetation stress estimation using surface energy balance approaches

https://doi.org/10.5194/egusphere-2026-4492
Preprint. Discussion started: 31 July 2026

(Olioso et al. 2020; Boulet et al. 2015; Olioso et al. 2013; Mallick et al., 2014, Bhattacharya et al., 2022). Its strength lies in capturing rapid changes in surface water status during dry-down periods following rainfall or irrigation, when ET responds nonlinearly to soil moisture depletion (Boulet et al., 2007; Delogu et al., 2012). Since albedo is a large contributor to the error budget of the energy balance calculation (Olioso et al. 2020), in addition to its spectral sampling in the VIS/NIR/SWIR domains, TRISHNA's orbital configuration and large field of view were designed to obtain at least three viewing angles every 8 days to constrain a directional model and improve the knowledge of reflectance anisotropy (Leon-Tavares et al. 2024).

The onset and propagation of pests and diseases such as desert locust (Nigam et al., 2026, rot-rust (Bhattacharya and Chatopadhyay, 2013) etc. in agriculture and forest ecosystems are often triggered through change in surface hydro-thermal conditions where noon-night LST play very important role. The delineation and persistence of coldwave and heatwave over crop fields can be monitored through high-frequent noon-night LST which form basis for agro-met advisory system (Bhattacharya and Nigam, 2024; Nigam et al., 2023). In addition, relative ET (ratio of ET and reference ET) and evaporative fraction from TIR-VNIR have been demonstrated to be an important input for crop yield estimation (Mallick et al., 2009; Bhattacharya et al., 2011). Plant mortality and phenological change due to higher soil and canopy temperature in forest ecosystem especially in Alpine (Chandra et al., 2022) is an important indicator of short-term climate change.

Crop water consumption and crop water productivity (ratio of yield or biomass or primary productivity and water seasonal or stage-specific water consumption) are the indicators of farm water footprint. Low water consumption but high crop water productivity indicates good performance of farm. Daily ET and its summation over a given period (season or stage) quantifies crop-soil system water consumption. Moderate-resolution high-repeat noontime thermal remote sensing and ET derived from surface energy balance were utilized to discriminate water consumption pattern of a variety of crops (Mallick et al, 2009). For optimized agricultural water management, it is necessary to decouple blue and green water consumption and productivity where irrigation is applied depending on rainwater availability. Independent estimate of ET from thermal remote sensing alongwith rainfall was used to estimate blue and green water consumption and productivity at coarser scale in India (Choudhury and Bhattacharya, 2021).

2.2 Monitoring of coastal and inland waters

Sea Surface Temperature (SST) and Lake Surface Water Temperature (LSWT) are designated as Essential Climate Variables (ECVs) by the Global Climate Observing System (GCOS). SST is fundamental for quantifying ocean–atmosphere exchanges and characterizing ocean circulation and biogeochemical processes (Donlon et al., 2009). In coastal regions, SST is closely linked to biological productivity when combined with indicators such as chlorophyll, turbidity, and suspended sediments (Behrenfeld et al., 2006; Li et al., 2003). Coastal regions exhibit strong spatial and temporal SST variability due to river plumes, estuaries, tidal mixing, upwelling, and sub-mesoscale dynamics (Huret et al., 2005; Chelton et al., 2007). These processes occur at scales of hundreds of meters to kilometers, requiring high-resolution observations (Capet et al., 2008; Fu and Ferrari, 2008). Their rapid temporal variability further demands frequent revisit (Baschek and Molemaker, 2010; Holt et al., 2012). Coastal and inland waters reflect climate variability and anthropogenic pressures (Reinart and Reynolds, 2008; Pour et al., 2012). They are both exposed to pollution, thermal discharges, and episodic disturbances affecting water quality and ecosystems (Grierson, 1998; Shih and Andrews, 2008; Pinel et al., 2013). In polar regions, sea-ice surface temperature controls ice extent, thickness, and climate feedbacks (Dean et al., 1994; Hall et al., 2004; Haggerty et al., 2003).

TRISHNA's high-resolution thermal infrared observations are suited to resolving strong thermal heterogeneity and rapid variability in coastal and inland waters. It will enable detection of narrow SST fronts and sharp gradients linked to river inputs,

https://doi.org/10.5194/egusphere-2026-4492
Preprint. Discussion started: 31 July 2026

estuaries, upwelling, and sub-mesoscale processes unresolved by current operational systems (Chelton et al., 2007; Holt et al., 2012). Frequent revisit and day–night acquisitions will capture transient thermal structures driven by turbulence and changing forcing. Due to reduced solar heating, night-time data will support air–sea flux studies (Donlon et al., 2009).

TRISHNA will fill a key observational gap for charaterizing sub-mesoscale phenomena (Kuroda et al., 2020, Tarantino et al, 2012; Thomas et al., 2002) andvalidating high-resolution ocean and coastal models by systematically observing fine thermal structures (Capet et al., 2008; Gutknecht et al., 2013). Applications include monitoring pollutant discharges, estuarine and wetland exchanges, freshwater resurgences, Sub-marine groundwater discharge (SGD), water quality, algal blooms, and fisheries support (e.g.Cahyono et al, 2017; Cheng et al., 2020; Mallast et al., 2013; Mejías et al., 2012; Perez et al., 2017). TRISHNA will enable unprecedented monitoring of thermal dynamics in inland waters improving our capacity to quantify and anticipate climate change impacts on aquatic ecosystems and biodiversity (Danis et al., 2004, Bayer et al., 2013; Daufresne et al., 2009), supporting sustainable management and restoration efforts. Complementary VNIR and SWIR observations will provide additional information on water color, enabling improved detection of surface algal blooms, turbidity, and suspended matter through reflectance-based indicators, particularly in optically complex coastal and inland waters (Matthews 2011; Trinh et al., 2017), even if quantitative retrievals remain challenging due to the broad specral bands compared to dedicated ocean color missions having narrow spectral bands.

2.3 Urban energy budgets and urban climatology

Anthropogenic activities and urban expansion generate strong spatial variability in urban microclimates and systematic temperature differences between cities and their rural surroundings, known as the Urban Heat Island (UHI) effect (Masson et al., 2020). Increasing heat-wave frequency under climate change poses major health and economic risks, driving demand for improved heat monitoring and early warning systems (Dousset et al., 2011; Chakraborty et al., 2015; Zhou and Shepherd, 2010; Masson et al., 2014). Among other solutions, vegetation can mitigate urban heat through shading and evapotranspiration while improving stormwater regulation (De Ridder and Lefebre, 2004; Maimaitiyiming et al., 2014). Accurate ET and LST estimates are therefore essential for urban water and energy budget assessment and for evaluating climate change mitigation strategies. LST also constrains urban atmospheric and air quality models (Quattrochi et al., 2006; Grimmond et al., 2011). Moreover, thermal infrared satellite observations are also central to characterizing UHI intensity and variability supporting heat stress evaluation (Voogt and Oke, 2003; Weng, 2009).

Urban climate is shaped by complex three-dimensional urban canopies and heterogeneous land use, which modify airflow, surface roughness, and surface–atmosphere energy exchanges (Arnfield, 2003; Voogt and Oke, 2003; Martilli et al., 2002; Masson, 2006). Artificial materials with diverse optical and thermal properties further alter urban energy budgets (Carlson and Arthur, 2000; Roberts et al., 2012). TRISHNA's high-resolution thermal infrared observations are well suited to capture urban heterogeneity, enabling consistent LST and ET measurements from neighborhood to city scales (Bechtel et al., 2012; Dominguez et al., 2011). The mission targets improved LST accuracy by addressing surface anisotropy, sub-pixel heterogeneity, and radiative interactions in complex 3D urban environments (Lagouarde et al., 2010a; Lagouarde et al., 2012, Roupioz et al., 2018).

Advances in temperature–emissivity separation and multi-band TIR analysis provide a strong basis for urban applications (Gillespie et al., 1998; Oltra-Carrió et al., 2014; Sobrino et al., 2012; Michel et al., 2021). Improved LST accuracy at TRISHNA spatial and temporal resolutions will support robust indicators of thermal comfort and population vulnerability (Stathopoulou and Cartalis, 2009; Mukherjee et al., 2016). The combined use with urban morphology and surface properties data will also

https://doi.org/10.5194/egusphere-2026-4492
Preprint. Discussion started: 31 July 2026

enhance characterization of urban energy exchanges, airflow, and heat storage (Masson et al., 2020, Keravec-Balbot et al., 2025), supporting fine scale Surface Urban Heat Island monitoring and heat-risk assessment for urban adaptation and mitigation policies.

2.4 Cryosphere

The cryosphere plays a critical role in global or local surface energy balance, hydrology, and climate feedbacks (IPCC, 2013; Benn and Evans, 2010). Snow surface temperature, emissivity, and albedo control radiative and turbulent fluxes, snow metamorphism, and melt timing (Gerland et al., 1999; Martinec, 1975; Singh and Singh, 2001; Kulkarni et al., 2006). These processes are essential for predicting runoff, flood risk, and seasonal water availability (Rathore et al., 2009; Singh et al., 2014).

Thermal infrared remote sensing provides key constraints for snow energy balance and melt models, particularly in data-sparse mountain regions (Hall et al., 1995; Hall et al., 2004; Kulkarni et al., 2006; Rathore et al., 2015). TRISHNA's high-resolution thermal infrared combined with VNIR–SWIR observations will improve estimates of snow surface temperature, emissivity, and albedo estimates, particularly in the mountainous regions, enhancing snow energy balance and melt modeling (Hall et al., 1995; Kulkarni et al., 2006). It will support monitoring of snow metamorphism through links between temperature, grain size, and albedo (Picard and Libois, 2024) and melt. A recent Observing System Simulation Experiment conducted by Alonso-Gonzalez suggests that the assimilation of TRISHNA LST strongly improves the modelling of the snow water equivalent (Alonso-Gonzalez et al., 2023).

Glacier monitoring is particularly challenging in debris-covered regions, where debris thickness strongly modulates melt rates (Benn and Evans, 2010; Rastogi and Ajai, 2013). Surface temperature measurements are essential for estimating glacier mass balance and assessing climate impacts, especially in high mountain Asia (Bhambri et al., 2013; Farinotti et al., 2015; Brahmbhatt et al., 2015). High-altitude lake temperature and ice phenology are also sensitive indicators of climate change (Hall et al., 2004).

High-resolution thermal data will also improve monitoring of glacier ablation zones and debris-covered ice by resolving temperature contrasts linked to debris properties (Gardelle et al., 2013).

2.5 Solid Earth

High-resolution thermal infrared (TIR) remote sensing provides access to key surface properties such as land surface temperature, emissivity and thermal inertia, supporting a broad range of solid Earth applications (Wooster and Rothery, 2000; Ramsey and Harris, 2013). Rock-forming minerals exhibit diagnostic emissivity features within the 8–12 µm atmospheric window, enabling lithological discrimination and geological mapping using multi-band TIR observations (Guha and Vinod Kumar, 2016). Combined day- and night-time acquisitions further allow estimation of thermal inertia, providing additional information on surface composition and physical properties (Ogawa et al., 2004). TRISHNA's multi-band observations in the 8–12 µm range, together with systematic day- and night-time acquisitions, will strengthen mineralogical mapping and thermal inertia retrievals at high spatial resolution.

TIR observations also play a major role in monitoring active geological processes and natural hazards. In volcanic environments, thermal anomalies can reveal magma ascent, degassing, lava effusion, and changes in volcanic activity between eruptive phases (Harris et al., 1997; Dehn et al., 2002; Antoine et al., 2020). Surface temperature anomalies have also been

https://doi.org/10.5194/egusphere-2026-4492
Preprint. Discussion started: 31 July 2026

investigated as potential precursors of seismic activity and, when combined with geodetic observations, may improve the monitoring of earthquake preparation processes (Tronin, 2010; Majumdar, 2013; Saraf et al., 2016). TIR measurements are furthermore essential for detecting volcanic ash and SO_2 plumes, supporting operational volcanic ash advisory systems (Prata, 1989; Realmuto et al., 1994; Watson et al., 2004; Carn et al., 2008; Prata, 2009). TRISHNA's high spatial resolution and frequent revisit will improve the detection and temporal monitoring of these thermal anomalies and complement SAR observations from missions such as NISAR for volcanic and seismic hazard assessment.

Beyond volcanology, TIR remote sensing contributes to geothermal exploration by detecting persistent thermal anomalies associated with geothermal fluid circulation, including in arid environments (Coolbaugh et al., 2007; Qin et al., 2011; Lopez et al., 2020). It is also used for detecting and monitoring persistent surface and subsurface fires, mapping landslides, identifying underground cavities through thermal anomalies, and revealing buried archaeological structures (Kuenzer et al., 2008; Roy et al., 2015; Fauchard et al., 2024; Edde et al., 2025). The combination of TRISHNA's high-resolution TIR observations with VNIR–SWIR data will enhance the characterization of these features and improve hazard assessment and geological mapping.

2.6 TRISHNA science team

The TRISHNA science team is structured around a set of dedicated thematic working groups, each focusing on a specific scientific domain addressed by the mission. These groups include scientists from multiple esearch institutions and universities. This international and interdisciplinary organization ensures that expertise in thermal infrared remote sensing, land surface processes, cryosphere dynamics, solid Earth applications, hydrology, agriculture, and coastal and ocean sciences is fully integrated. Close interaction between scientists and space agency teams supports the definition of mission requirements, calibration and validation strategies, algorithm development, and product assessment. In addition, the science team actively considers the strong synergy between TRISHNA and forthcoming thermal missions LSTM and EAGLE-TIR, enabling cross-mission consistency, products intercomparison, and enhanced spatio-temporal sampling.

3 TRISHNA mission design

3.1 High-level mission requirements

Lifetime

TRISHNA’s 5-year lifetime guarantees several full seasons of observation. This makes possible the observation of contrasts between successive years. Moreover, the longer the time in operations, the higher the chances to observe contrasted years for a given location, and possibly to document trends representative of expected changes related to global warming and climate drifts. Moreover, a longer life in orbit will favor a longer overlap period with following missions such as LSTM and EAGLE-TIR, for a better interoperability and revisit time. Therefore, consumables will be available for a mission extension of minimum 2 years.

Near-Real-Time evapotranspiration (ET) for irrigation decisions

Irrigation management benefits from having ET information with short latency (near-real-time or frequent updates) for the following reasons: (i) Irrigation scheduling precision: Frequent ET estimates help match water applications with actual crop water requirement (Corbari and Mancini, 2023); (ii) Water use efficiency: Accurate short-term ET allows for implementing Deficit Irrigation practices while preventing water logging (Wang et al. 2023, Yu et al. 2020); (iii) Adaptive decision systems: Automated and sensor-based irrigation systems require up-to-date ET to trigger irrigation thresholds and dynamic water allocation (Garcia et al. 2020, Lakhiar et al. 2025); and (iv) Forecast irrigation: Short-term ET forecasts allow planning ahead

https://doi.org/10.5194/egusphere-2026-4492
Preprint. Discussion started: 31 July 2026

for irrigation needs under changing weather conditions (Han et al., 2022). Therefore, in order to demonstrate the operational use of the products for irrigation management, level 2 and 3 products will be delivered to the users 12 hours (goal) after the acquisition (as one says, "before the farmer's breakfast"). Therefore, areas with high percentage of irrigated fields will be targeted for this real-time production.

A free and open data policy

TRISHNA data will be available with a full free and open data policy, in accordance with the Copernicus data and information policy of the European Union (European Commission, 2014; Regulation (EU) No 377/2014) as well as in accordance with Indian space policy, 2013 (https://www.isro.gov.in/media_isro/pdf/IndianSpacePolicy2023.pdf). The free, full and open access to TRISHNA data and Service information will stimulate the development of Science, Public Utility and Commercial Applications.

3.2 Specifications driving orbit selection

3.2.1 Global coverage

Since the regions and sites addressed by the scientific themes – and particularly the two drivers: continental biosphere and coastal and continental water – are distributed all over the Earth, global coverage is required. Studies related to climate change only make sense if considered globally. Thus, the mission will provide global accessibility of all continental and coastal areas on the Earth Surface from a single platform.

3.2.2 Revisit time

The geometric access time, also referred to as the revisit time, is defined as the temporal periodicity of systematic acquisitions over a given area, independently of cloud cover.

Global coverage will be achieved with a single satellite while maintaining a reasonable maximum viewing angle, limiting anisotropy effects, and avoiding excessive pixel distortion. The revisit time therefore results from an optimal trade-off between scientific requirements and geometric feasibility. From a geometric standpoint, revisit times shorter than three days would require unrealistically large swath widths to ensure global coverage: a two-day revisit (altitude 720 km) would necessitate viewing angles of approximately ±42°, while a one-day revisit (altitude 560 km) would require angles of approximately ±62°, which would lead to unacceptable radiometric and geometric distortions.

The scientific requirements guiding the selection of the revisit time are detailed in the following subsections and include: (i) ensuring sufficient availability of cloud-free observations; (ii) achieving the required accuracy of derived geophysical products; and (iii) properly accounting for uncertainties in surface measurements.

3.2.3 Providing sufficient availability of cloud-free data

For evapotranspiration retrieval, Land Surface Temperature observations are ideally required at a daily temporal resolution (Lagouarde et al., 2010b). This requirement may be relaxed to a minimum revisit interval of three days with limited impact on ET estimates (Lagouarde et al., 2013; Sobrino et al., 2016, Guillevic et al. 2019). However, a daily geometric revisit does not translate into daily usable observations due to cloud obstruction. Cloud occurrence is strongly dependent on geographic location and seasonal variability. Consequently, cloud climatology must be jointly analyzed with local crop calendars to optimize the effective revisit requirement: Lagouarde et al. 2010, evaluated the data availability from a statistical analysis of an 18 years meteorological data base over 3 sites in France. Assuming 1 clear day is necessary by 5 day-periods for monitoring water budgets, the study revealed that this criterion can be fulfilled all year long only with a 1 day revisit. Furthermore, in the same article, the analysis of MODIS data (1 km resolution) on western Europe for spring and summer showed that, excepted

https://doi.org/10.5194/egusphere-2026-4492
Preprint. Discussion started: 31 July 2026

for southern Europe countries, the average length of periods without data varied on a range between 5 and 10 days for a 1 day revisit, but may reach up to 20 days for a 2 day revisit.

These considerations lead to a requirement on revisit time from 1 (goal) to 3 days (threshold).

3.2.4 Providing sufficient accuracy on derived products

Revisit frequency combined with cloud occurrence can be a strong limitation on the accuracy of ET monitoring (Lagouarde et al., 2010b, Guillevic et al., 2019, Alfieri et al. 2017). The determination of daily ET on days without available acquisition requires the implementation of temporal interpolation/extrapolation procedures. In most cases, a simple linear interpolation of the ratio between ET and a known scaled metric was performed (Delogu et al. 2012, Alfieri et al. 2017, Guillevic et al. 2019): the reference metric may correspond to incoming solar radiation, extra-terrestrial solar radiation or reference evapotranspiration. More complex methodologies that enable to integrate other information, such as rainfall, meteorological reanalysis data, ET model simulations or surface soil moisture, are under study based on fusion methodologies or signal filtering (Allies et al. 2022, Delogu et al. 2021, Farhani 2022). At present, such methodologies cannot be used as a basis for interpolation procedures in operational high–spatial-resolution systems, as they have not yet been adequately evaluated in the international literature.

When considering simple interpolation procedures, most of the studies cited above showed that the incoming solar radiation at the Earth surface provides the best tradeoff between simplicity and performances.

Olioso et al. (2022 and 2023) evaluated the uncertainty related to the interpolation processes first as a function of revisit and second by considering TRISHNA potential orbital characteristics showing strong improvement in the performances when increasing the revisit (Fig. 1) and when comparing TRISHNA to LANDSAT estimates (Fig. 2).

Figure 1 also shows that a 3-day revisit achieves good performances in terms of uncertainty. It was therefore considered as a threshold requirement for TRISHNA.

https://doi.org/10.5194/egusphere-2026-4492
Preprint. Discussion started: 31 July 2026

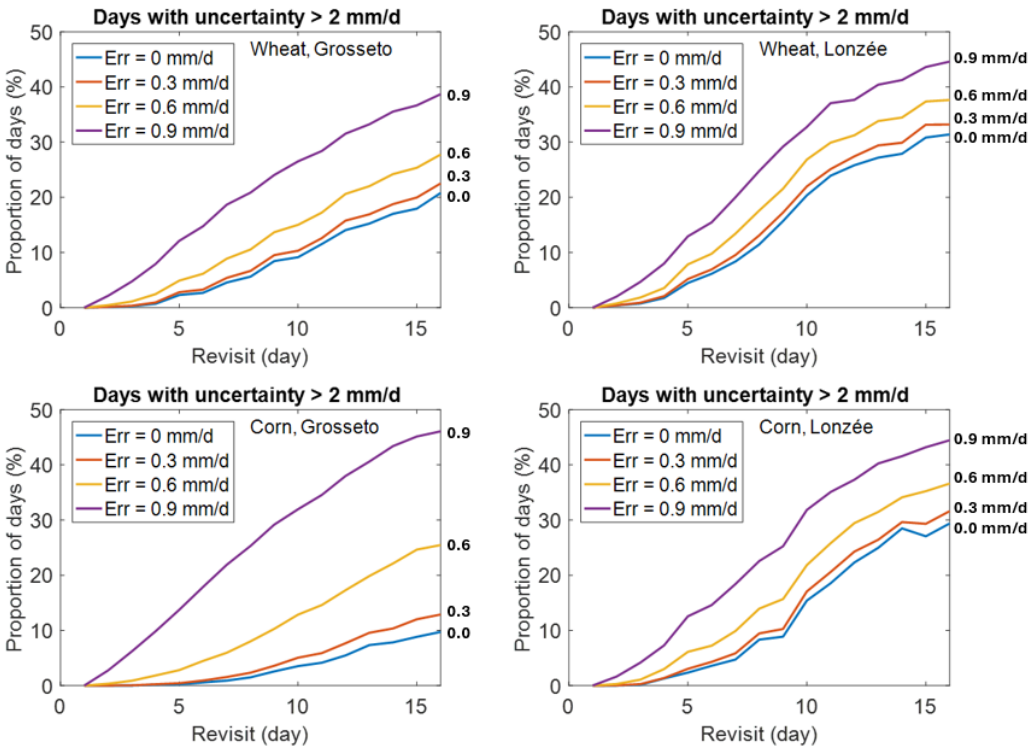

Figure 1 Proportion of days for which the uncertainty related to the interpolation procedure is higher than 2 mm/d for corn and wheat crops in Grosseto, Italy, and Lonzée, Belgium, as a function of revisit and error level in ET estimation, adapted from Olioso et al. 2022

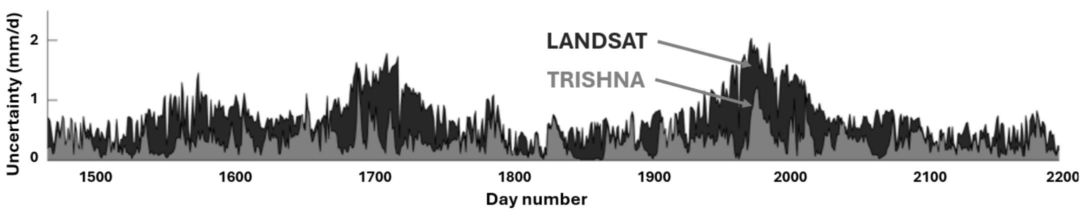

Figure 2 Daily ET uncertainty for a C3 crop in Grossetto, Italy, over two years, for TRISHNA in red, and LANDSAT, in dark blue. Daily ET is interpolated considering incoming solar radiation, adapted from Olioso et al., 2023

3.2.5 Dealing with uncertainties of surface temperature measurements

Accounting for uncertainties inherent to surface temperature retrievals is essential, particularly in minimizing the impact of atmospheric turbulence on instantaneous thermal infrared observations.

Turbulent motions occurring in both the surface boundary layer (SBL), which is directly controlled by exchanges of heat and moisture between the land surface and the atmosphere, and the planetary boundary layer (PBL), whose evolution is primarily driven by the daily cycle of surface heating and cooling, produce pronounced temporal variations in surface temperature. These turbulent processes act over two distinct temporal scales that have different implications for thermal infrared observations but

https://doi.org/10.5194/egusphere-2026-4492
Preprint. Discussion started: 31 July 2026

are often not explicitly distinguished. At short time scales, high-frequency temperature fluctuations are primarily associated with small-scale turbulent eddies. Their impact on satellite retrievals can be substantially reduced through temporal averaging or by the spatial averaging inherent to the dimensions of the sensor pixel. In contrast, larger-scale turbulent structures generate abrupt shifts between quasi-stationary temperature states, producing step-like changes in the observed surface temperature. Because these fluctuations occur at scales comparable to or larger than the sensor footprint, they cannot be effectively mitigated by pixel averaging and therefore introduce an irreducible uncertainty in instantaneous thermal infrared retrievals (Lagouarde et al., 2013). Reducing this source of uncertainty requires observations with improved temporal sampling, enabling a more complete characterization of the evolving thermal state of the surface–atmosphere system.

This provides a strong physical rationale for high revisit frequency missions such as TRISHNA. However, the magnitude of this improvement remains difficult to quantify, as it depends on the amplitude and temporal spectrum of temperature fluctuations, both of which are highly site-specific and generally poorly constrained without dense ancillary observations.

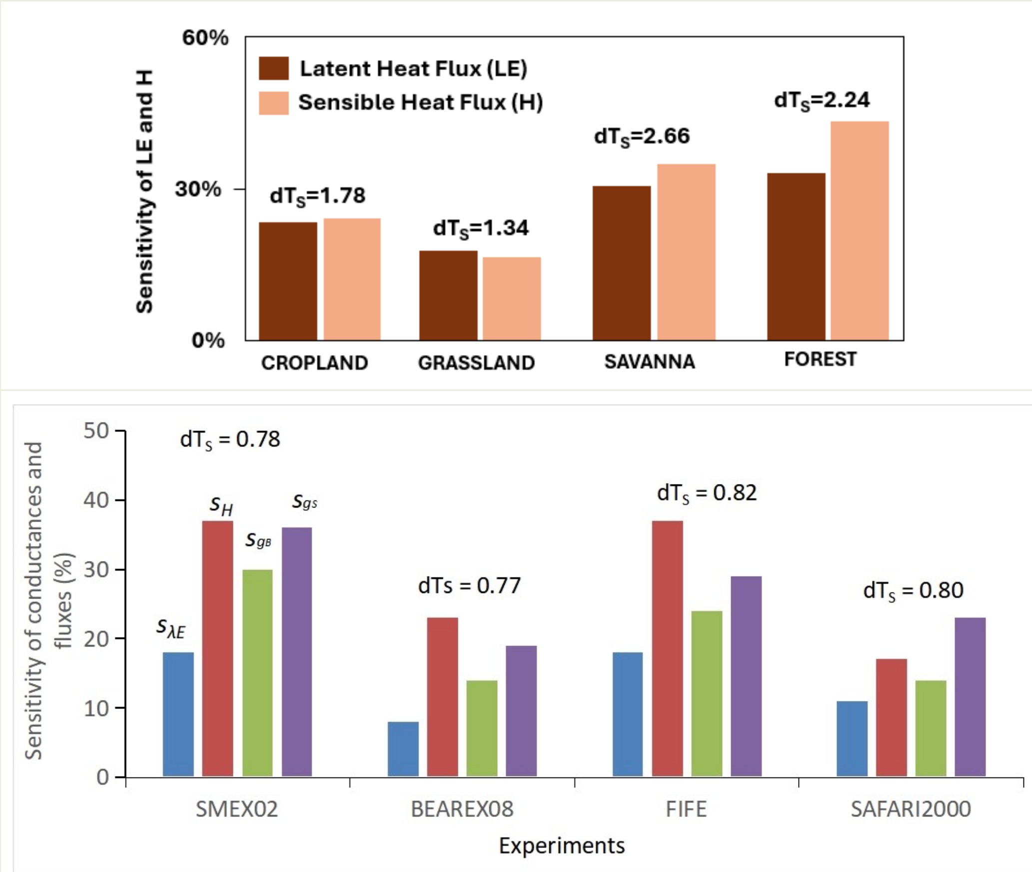

Figure 3: (a) Sensitivity of STIC (Surface Temperature Initiated Closure) derived latent and sensible heat fluxes to land surface Temperature uncertainties across different biomes, adapted from Mallick et al. (2014); (b) Sensitivity of STIC biophysical conductance (gB and gS) and surface energy fluxes (λE and H) to land surface temperature uncertainties, adapted from Mallick et al. (2015).

Uncertainty in LST propagates directly into surface energy flux estimates. Simulations using the analytical surface energy balance model STIC (Surface Temperature Initiated Closure) (Mallick et al., 2014) show that LST uncertainties of 1.3-2.2 K,

https://doi.org/10.5194/egusphere-2026-4492
Preprint. Discussion started: 31 July 2026

across different land cover types, can lead to uncertainties of approximately 24-33% (for latent heat flux, LE) and 17-44% (for sensible heat flux, H) (Fig. 3). Using another version of STIC, a follow-up study (Mallick et al., 2015) also revealed substantial sensitivity of the biophysical conductances and fluxes to random uncertainties in LST. Using data from different surface flux experiments, this study reported sensitivity of stomatal conductance and aerodynamic conductances to account for 20 - 35% and 15 - 30% for 0.75 - 0.82 K uncertainty in LST. The corresponding sensitivity in LE and H was of the order of 10 - 18% and 20 - 35%, respectively. These results underline the critical need to better characterize and reduce LST uncertainties for reliable estimation of land-atmosphere exchanges.

3.2.6 Observation angles and directional anisotropy

Revisit time under the same viewing configuration: the geometric revisit time under the same viewing direction (temporal periodicity of systematic acquisition of a given area disregarding cloud cover and under the same viewing direction) will not be longer than 8 days, as the capability of a system to capture rapid changes in ET is significantly reduced for return periods higher than 8 days (Guillevic et al., 2019).

With a constant view angle, multi-temporal observations on a given site can be compared with better accuracy by considering directional effects as a constant bias, thus removing from the error budget the uncertainties associated to the modeling of the directional effects.

Observation angle limit: the Observation Zenith Angle (OZA) is the angle between the satellite viewing vector and the local zenith at the observation point.

OZA shall remain below a threshold value in order to limit the increase in pixel size caused by off-nadir viewing conditions, and to reduce atmospheric correction errors associated with the increased optical path length through the atmosphere.

The requirement on maximum OZA has been set to 40 degrees in order to: (i) avoid excessive enlargement and geometric distortion of pixels; and (ii) limit atmospheric correction errors by reducing the apparent thickness of the atmospheric layer. In addition, surface emissivity exhibits angular dependence, particularly over heterogeneous and anisotropic surfaces, which can introduce additional uncertainties in thermal infrared retrievals at large viewing angles.

Accounting for directional anisotropy: directional effects occur because satellite observations integrate temperatures from different surface components within a pixel. Changes in viewing geometry modify the relative proportions of sunlit and shaded elements and surfaces with different emissivities. Two key mechanisms drive these effects: the hotspot effect, where alignment of solar and viewing directions increases the proportion of visible sunlit elements and raises apparent temperature, and the gap fraction effect, where viewing angle alters the relative proportion of vegetation and soil in the field of view. These phenomena can introduce temperature variations of several degrees, potentially compromising the detection of environmental indicators such as crop water stress. On the other hand, large view angles can also bring opportunities to target more specifically the canopy (Mwangi et al., 2022).

In the optical domain, the hotspot effect has been well characterized from both the experimental and modeling point of view (Roujean, 2000, Qin et al., 1995). In the TIR domain, different parametric models are available: the Ross-Li model (Roujean et al., 1992; Wanner et al., 1995; Ren et al., 2014), the LSF-Li model (Su et al., 2002), the Vinnikov model (Vinnikov et al., 2012), the RL model (Lagouarde and Irvine, 2008; Duffour et al., 2016), the LSF-RL model (Cao et al., 2021).

As an attempt to quantify these effects, Michel et al., 2023 combined near-nadir observations from Landsat 8 with wide-angle measurements from the airborne MODIS/ASTER Airborne Simulator (MASTER). Nine quasi-simultaneous acquisitions were

https://doi.org/10.5194/egusphere-2026-4492
Preprint. Discussion started: 31 July 2026

analyzed to examine directional behavior and evaluate several existing parametric models designed to correct TIR anisotropy. The results show that directional temperature differences across viewing angles range from 1.6 K to over 6 K, particularly under hotspot conditions. Applying the five aforementioned correction models significantly reduced these errors. Corrected temperatures showed reductions in root mean square error (RMSE) of 0.2–0.9 K, and the amplitude of directional effects decreased to below 1 K in most cases. Global models fitted across all datasets also reduced RMSE and directional error budgets, typically bringing them below 2 K.

As a consequence, the following strategy will be applied to TRISHNA:

- Observation time series for a given location will systematically include acquisitions that are not affected by hot spot conditions. This implies allowing observations of the same location under different viewing geometries so that measurements are not systematically contaminated by hotspot effects over several consecutive observations.
- Short revisit times at constant viewing angles will be maintained: to minimize the influence of directional anisotropy in operational products, the requirement of maintaining a revisit time at constant viewing angles shorter or equal to 8 days is introduced, as this value is identified by Guillevic et al., 2019 as a critical threshold, beyond which rapid surface moisture changes are poorly captured. This temporal constraint allows analyses under comparable observation geometries, especially considering that cloud cover may further reduce the number of usable observations.
- User information on degraded performance near hotspot configurations: whether a directional correction is applied or not, it is important to inform end users about potential performance degradation near hotspot configurations. This is achieved by introducing a quality flag in the data products, indicating when observations are likely affected by strong directional effects and when the associated uncertainties may be higher.

Nevertheless, continued research is required to improve the modeling and correction of directional effects in the thermal infrared domain. In particular, in-orbit calibration and validation (Cal/Val) activities will be pursued, including dedicated airborne or ground-based measurement campaigns during satellite overpasses. These efforts, combined with the data provided by TRISHNA, will support the refinement of existing parametric models and facilitate their potential operational implementation in ground processing chains for future TIR missions.

3.2.7 Ground sampling distance (GSD)

Level 2 products will combine information from both visible-NIR and TIR cameras, thus the merging of both samplings drives directly the final characteristics of the product. The upper limit of GSD for land and coastal areas is driven by typical size of the ground units (fields) of the studied areas. The lower limit of resolution is driven by technological constraints and by the uncertainty due to the turbulent nature of the surface temperature, especially above vegetation.

Upper limit of the ground resolution

The upper limit of GSD is mainly driven by the following aspects: typical size of fields, possibility to separate different types of crops for a given land use, possibility to assess UHI events.

It is obviously difficult to propose a unique value, as it depends on the type of landscape studied. Nevertheless, we can refer to Kustas et al., 2004 who studied the resolution necessary to separate the contribution to actual evapotranspiration of 2 crops, soybean and corn in the Iowa plain where fields range in size between 1 to 150 ha, with a typical size of 25 ha. Both crops can be well separated at 60 m resolution (Fig. 4). India's field size is less, typically around one hectare. Therefore, a resolution of less than 60m is advised.

https://doi.org/10.5194/egusphere-2026-4492
Preprint. Discussion started: 31 July 2026

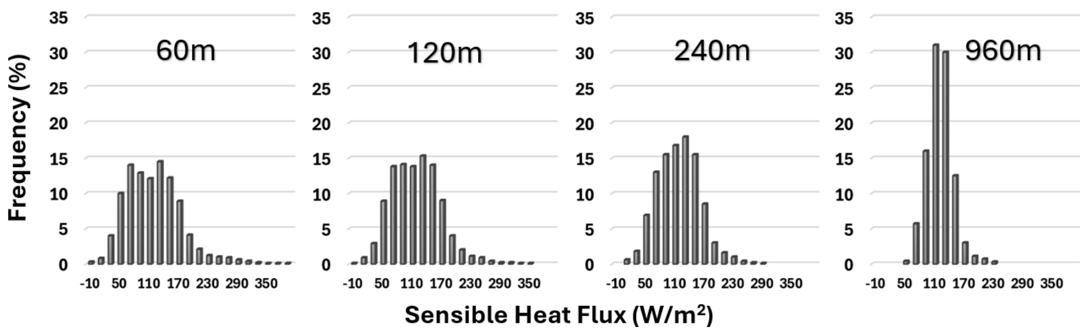

Figure 4 Histograms for the sensible heat flux distributions over corn and soybean fields in Iowa at different resolutions for July 1, 2002, Landsat 7 overpass. Flux interval is 20 W.m^{-2} (adapted from Kustas et al., 2004)

In the case of Texas high plains where the typical size of field is ~800x800m, Agam et al. 2007 show that a resolution ≤100m is optimal for agricultural applications: such a resolution allows to resolve differences between fields, and within fields satisfactorily.

A similar conclusion was found by Garrigues et al. 2006 who quantified the spatial heterogeneity of the NDVI for 18 landscapes of the VALERI (Validation of Land European Remote sensing Instruments) database (Baret et al., 2021) and similarly concluded that 'the sufficient pixel size to capture the major part of the spatial variability of the vegetation cover at the landscape scale is estimated to be less than 100m'.

In France, geographic agricultural parcel database is produced annually from farmer declarations under the Common Agricultural Policy (PAC), managed by the Agence de services et de paiement (ASP) and disseminated via the Institut national de l'information géographique et forestière (IGN). The data is openly available through data.gouv.fr and IGN geoservices. Such a work was done using data gathered in the French Gers department, which is a typical hilly agricultural region in South-West of France (Fig. 5).

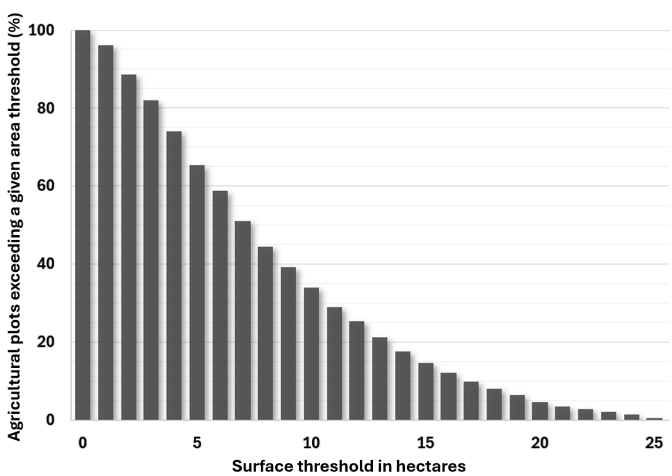

Figure 5 Envelope of cumulative histograms of plot surfaces, obtained for 4 types of crops (corn, wheat, rapeseed, sunflower) in Gers department in France, based on farmer declarations. Statistics are based on 80 000 plots, source data downloaded from www.data.gouv.fr/datasets/rpg

https://doi.org/10.5194/egusphere-2026-4492
Preprint. Discussion started: 31 July 2026

Typically, the histogram shows that for the main crops, 82% of the surface is made of plots greater than 3 ha, i.e. corresponding to a 3x3 grid of 60m pixels.

The above-mentioned studies show that resolutions finer than or equal to 100 m are needed to reliably separate different crops, resolve field-to-field variability, and capture most vegetation and heat-flux heterogeneity at landscape scale. Coarser resolutions would merge many agricultural plots into single pixels, reducing the ability to distinguish land use, crop type, and UHI-related spatial patterns. Thus, the maximum value for the ground sampling distance is set to 100 m.

Turbulence and lower limit of the ground resolution

The surface temperature displays temporal fluctuations of different frequencies related to turbulence (Lagouarde et al., 2015):

- Turbulence related to surface boundary layer (high frequencies) corresponds to turbulent structures of a few meters and can be smoothed by the spatial integration at the pixel scale (the so-called 'ergodicity')
- Turbulence in the convective planetary boundary layer (low frequencies) corresponds to turbulent structures of a few hundreds meter in size. It cannot be smoothed out and contributes to the uncertainty on the surface temperature measurement.

Lagouarde et al., 1997 analyzed the results of experiments performed on August 16, 1995 over maritime pine stands in Le Bray Carbo-Europe INRAE site, using a helicopter-borne TIR camera. Aggregated pixel sizes are 5 m, 19 m and 200 m. Their observations show that the temporal evolution of the surface temperature over a 600s period exhibits low frequency fluctuations related to convection in the PBL. These fluctuations remain present whatever the spatial resolution considered, while high frequency fluctuations are smoothed by spatial integration as the pixel resolution decreases. This indicates that for resolutions finer than 35 to 40 m, the overall performance will be limited by these high frequency fluctuations.

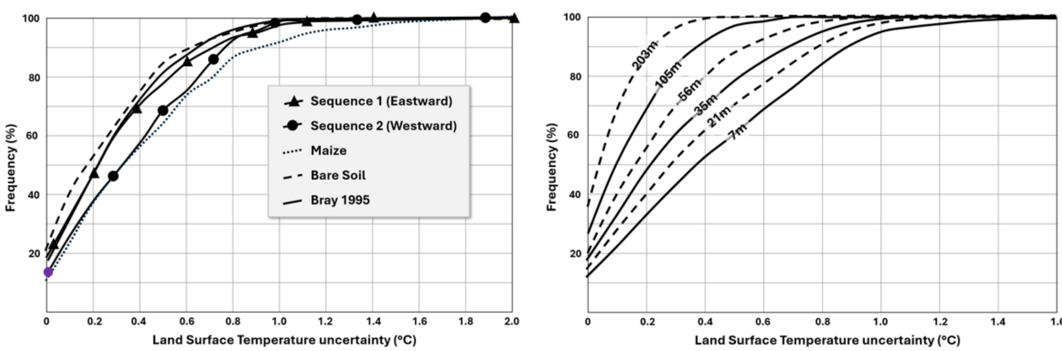

Figure 6 Statistics of satellite LST deviations from the mean were computed over two 20-min acquisition sequences (Seq. 1 eastward, Seq. 2 southward) above a pine stand at 50 m spatial resolution (left), and across multiple resolutions for a 3 × 3 km LES-simulated domain under the ergodicity assumption (right). These statistics represent the frequency distribution of errors in surface temperature measurements. (adapted from Lagouarde et al. 2015)

Furthermore, Lagouarde et al. 2015 analyzed the maximum cross-correlation between LST and wind speed over maize crops and concluded that wind exerts dominant control on temporal fluctuations in LST, while no significant correlation was found with air temperature. In the same article, Fig. 7 shows that the amplitude of the LST temporal fluctuations decreases with spatial resolution.

https://doi.org/10.5194/egusphere-2026-4492
Preprint. Discussion started: 31 July 2026

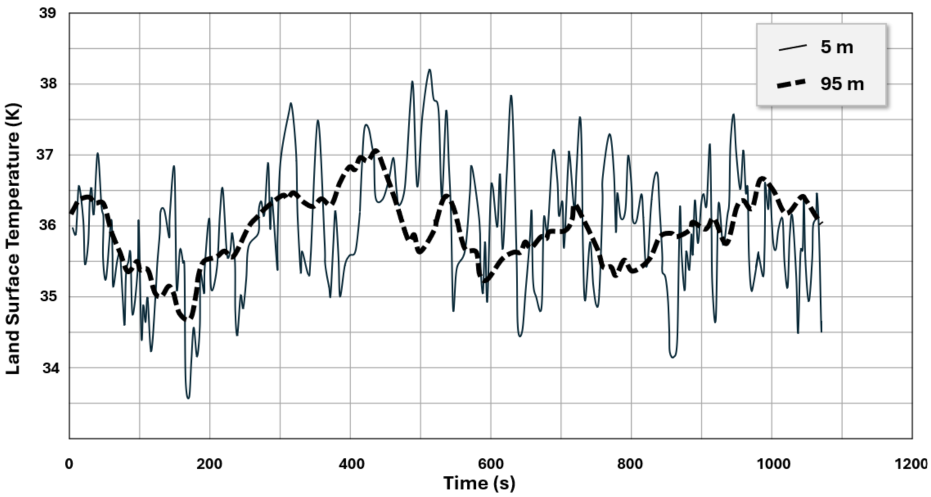

Figure 7 Spatial integration effects on small-scale LST variability: temporal evolution over a maize canopy, adapted from Laouarde et al. 2015

Spatial resolution is also critical for assessing Urban Heat Island events. Sobrino et al., 2009 analyzed the thermal pattern over Madrid city at different spatial resolutions simulated from an airborne (AHS) image with a pixel size of 4 m (DESIREX campaign 2008). It can be observed that thermal pattern over the city is still accurate for resolution of 50 meters but degrades at 100m.

Thus, the requirement on the lower limit of ground sampling distance is set to 50 meters.

3.2.8 Local Time considerations

Selecting an appropriate satellite overpass time is critical for accurate surface flux estimation.

Analyses of cloud cover indicate that acquisitions between 10:00 and 14:00 are much less affected by cloudiness, based on radiation measurements from French meteorological stations and MODIS cloud masks over Europe (Lagouarde et al., 2010b), suggesting that cloudiness does not strongly limit midday observations. **Stability of vegetation variables and albedo** further supports midday measurements, as noon-time values of vegetation indices and land surface albedo have minimal influence on flux retrievals. **Maximum sensitivity of fluxes to surface temperature** occurs near midday, particularly for actual evapotranspiration, a pattern confirmed by coupled SVAT–boundary layer simulations showing latent heat flux maxima around 13:00 local time (Gentine et al. 2007; Mallick et al., 2009), which enhances signal-to-noise ratio and retrieval accuracy.

Minimizing angular effects is an additional advantage, as higher solar elevation reduces directional biases in emissivity and reflectance at mid-latitudes (Lagouarde et al., 2010b). **Relaxation of overpass time constraints** is also achieved, since small deviations around midday have limited impact, facilitating comparisons with numerical models on 30-minute to hourly time steps. **Temporal scaling to daily fluxes** is improved because noon-time measurements accurately represent the amplitude of the diurnal cycle.

Night-time acquisitions benefit from a midday or early-afternoon overpass, positioning observations near the middle of the night and well away from sunset, which is important for coastal and inland SST studies.

https://doi.org/10.5194/egusphere-2026-4492
Preprint. Discussion started: 31 July 2026

Operational constraints, including launch compatibility and spacecraft power limitations, restrict feasible local times to before 13:30. Finally, **harmonization with sister missions** provides nearly simultaneous measurements at similar solar angles and supports long-term continuity with COPERNICUS LSTM datasets.

Accordingly, the mission will follow a Sun-synchronous orbit with a mean local time of descending node of 12:30 PM.

3.2.9 Orbit selection methodology

The requirements on the orbit are summarized in Table 1:

Coverage	Global
Revisit	1 to 3 days
Revisit with same geometrical configuration (hot-spot free)	Maximum 8 days
Mean Local time	12:30 PM +/- 15mn (Descending Node)
Ground sampling distance	50 to 100 m
Maximum OZA	40 degrees

Table 1 Requirements on the orbit

As an attempt to limit the pollution of the datasets by the proximity with the hotspot geometric configuration, it was decided to take advantage of the sub-cycles of the orbit, so that during the repeat cycle of the orbit, each location is observed *n* times from different tracks, i.e. with different view angles. This ensures that (*n*-1) observations per orbital cycle are not affected by the hotspot. To access these subcycles globally, the swath is extended, and consequently the OZA. So we looked for a phased orbit with a cycle lower or equal to 8 days, sub-cycles equal or lower than 3 days, and a maximum OZA of 40 degrees.

Table 2 provides the characteristics of the phased orbits with a cycle of 3 to 8 days and sub-cycles not exceeding 3 days, computed from a purely geometrical aspect, with a spherical Earth assumption. In the (n,p,q) convention used to define the orbit, n is the integer number of revolutions per day (typically 13–15), p is the repeat cycle in days, and q is the remainder of the division such that the actual mean motion is n + q/p, leading to a total of np+q revolutions over the repeat cycle.

n	p (cycle)	q	Number of tracks per cycle	sma (km)	Period (sec)	Altitude (km)	Intertrack (km)	Subcycles	Max OZA (deg)
14	3	1	43	7145.71	6011.45	775	466.0	3	34.9
14	3	2	44	7037.03	5874.82	666	455.4	3	38.1
14	5	2	72	7123.64	5983.62	753	278.3	3-2	40.9
14	5	3	73	7058.43	5901.65	687	274.5	3-2	42.9
14	7	2	100	7161.58	6031.49	791	200.4	3-1-3	41.9
14	7	3	101	7114.23	5971.77	743	198.4	2-3-2	43.3

https://doi.org/10.5194/egusphere-2026-4492
Preprint. Discussion started: 31 July 2026

14	7	4	102	7067.66	5913.22	697	196.4	2-3-2	44.7
14	8	3	115	7131.90	5994.02	761	174.2	3-2-3	38.7
14	8	5	117	7050.39	5891.56	679	171.3	3-2-3	41.2

Table 2 Characteristics of the phased orbits with a cycle of 3 to 8 days and sub-cycles not exceeding 3 days, computed from a purely geometrical aspect, with a spherical Earth assumption.

The only orbit of the table exhibiting a maximum OZA below 40 degrees and different view angles is the (14,8,3) 8-day orbit (115 orbits per repeat cycle), at the altitude of 761 km.

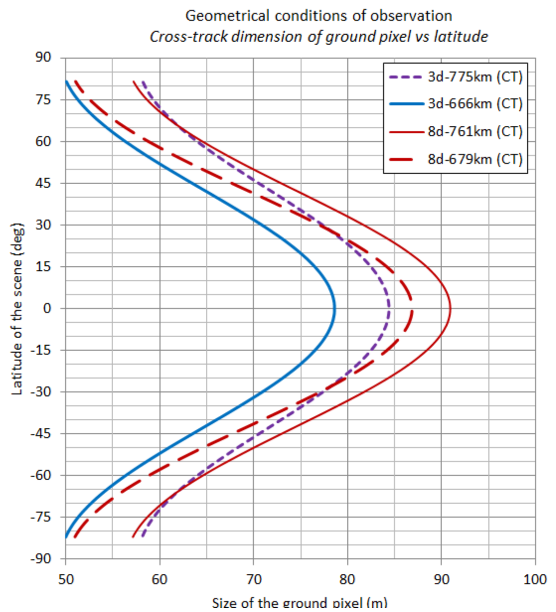

Figure 8 Variation of the GSD within the swath of the candidate orbits

As the instrument was initially designed for a resolution of 50 m at nadir on the phase A 3-day cycle / 666 km orbit, a higher orbit implies an increase of the GSD. It varies across the swath, ranging from 57 m at nadir to 91 m at the edge of the swath. A product resolution of 60 m was chosen to obtain a round number while maintaining the highest possible resolution for users. Indeed, choosing a product resolution close to that at the swath edge would result in a loss of information across most of the swath compared to the native resolution.

This remains fully compatible with the minimum ground resolution requirement for TRISHNA. The product resolution will be as close as possible to the lower limit as set by the scientific community, mainly driven by atmospheric turbulence.

The GSD will be lower than the maximum allowed value (100 m) even at the edge of scan.

It should be noted that the computed edge of scan GSD corresponds to the extension of the pixel size in the cross-scan direction (CT). As the extension of the pixel size in the long-scan direction (LT) is of lower amplitude, the pixel surface at the edge of scan is lower than CT^2. Furthermore, the actual pixel area shall be computed considering the alteration of the pixel shape due to the geometry of the acquisition.

https://doi.org/10.5194/egusphere-2026-4492
Preprint. Discussion started: 31 July 2026

3.3 Spectral Requirements

3.3.1 On the need for simultaneous TIR, VNIR and SWIR acquisitions

In the context of the TRISHNA mission, the need for VNIR acquisitions concomitant with the TIR is justified by the following factors:

- **register VNIR and TIR images**. On the platforms foreseen for TRISHNA, attitude data will not be accurate enough to provide a sub-pixel accuracy for the registration of TIR images, without ground control points. Previous missions have shown that the ground control points will be more accurate if automatic matching is applied in the visible rather than in the TIR.
- **detect high thin clouds** using a SWIR band, where water vapor absorbs all the light when the ground altitude is below 2000 m for standard water vapor conditions (Gao et al. 1995).
- **Separate Snow from Clouds**: snow is very dark in the SWIR while clouds stay bright. The SWIR band allows us to discriminate these categories.
- **estimate aerosol optical depth** using SWIR, red and blue band combinations. Estimation the AOD allows us to better estimate the downwelling irradiance.
- **Identify land cover**. Visible bands are well adapted to determine the type of surface observed, which is necessary for some of the algorithms used to derive fluxes.
- obtain a **first guess for emissivity** from the vegetation cover. VNIR spectral bands provide vegetation indexes that are often used in Temperature/Emissivity separation algorithms. Presence or absence of vegetation is one of the main factors of emissivity variations.
- **estimate albedo** to determine net radiation which drives land surface evapotranspiration.
- **estimate biophysical variables of vegetation** (Leaf Area Index, LAI, and fraction cover, Fcover) which are mandatory to compute surface fluxes (evapotranspiration in particular) in combination with LST
- SWIR band will also be used to detect vegetation stress and burnt areas (Gerhards et al., 2019), as well as to compute soil moisture parameter in the single-pixel evapotranspiration computation (Mallick et al., 2015). Although LST is a direct indicator of plant water stress under a given radiative and environmental forcing, its interpretation is not unique. An increase in LST may result from stomatal closure due to physiological water stress, but also from non-physiological factors such as weak aerodynamic coupling under low wind conditions or the influence of hot soil in sparsely vegetated canopies. These eco-physical situations can be better distinguished by combining LST with SWIR reflectance. Water strongly absorbs radiation in the SWIR domain, particularly around 1600 nm and 2100-2200 nm. Under well-watered conditions, high liquid water content in leaves and soil leads to strong absorption and low SWIR reflectance. As water stress develops and water content declines, absorption weakens and SWIR reflectance increases. This response is largely independent of stomatal behavior, as it directly reflects the water content of the soil-canpoy complex. LST and SWIR thus provide complementary information. LST reflects the energetic or thermal response to stress through reduced transpirational cooling, while SWIR captures the underlying change in water content that drives this response. Together, they constrain both the effect and the cause of vegetation water stress. In this context, the near-infrared (NIR) region serves as a reference, while SWIR reflectance decreases with increasing moisture content. Combining NIR and SWIR enhances sensitivity to variations in liquid water. When used together with LST, this synergy provides a robust signal to better capture water stress effects on evapotranspiration and ecosystem functioning.

Image registration, cloud detection and estimation of water vapor require near simultaneity of acquisitions between the VNIR and TIR images, which makes it impossible to rely on another sensor in the VNIR.

https://doi.org/10.5194/egusphere-2026-4492
Preprint. Discussion started: 31 July 2026

Simultaneity between TIR and VNIR is also demanded to assess vegetation status, identify land cover and estimate emissivity and albedo, because using data from another satellite would lead to an often outdated information on vegetation status, and consequently a reduced accuracy. For instance, the theoretical cycle of Sentinel 2 is 5 days (obtained with 2 satellites), but concretely much less given the cloud cover.
Given the dynamics of the processes involved, simultaneity is considered sufficient if TIR and VNIR-SWIR data are acquired within a typical delay of a few seconds. However, as the data will be acquired from different viewing angles, parallax effects on clouds must be considered during image registration and analysis.

3.3.2 Definition of TIR Spectral bands

The positioning of TIR spectral bands in the 7.5 µm to 13 µm spectral range for satellite-based LST retrieval has been the subject of several studies (Caseles et al., 1998; Sobrino et al., 2010; Sobrino and Jimenez-Munoz, 2014; Jacob et al., 2021). These studies have shown that optimal positioning of TIR bands for a LST-driven mission such as TRISHNA must be based on considerations regarding (i) atmospheric absorption, (ii) surface emissivity contrast, (iii) instrumental noises, and (iv) the LST retrieval methods selected for the mission.

Regarding atmospheric absorption, TIR bands are located in spectral regions with the highest atmospheric transmission, since in these cases the effect of the atmosphere on the measurements is minimized. In the TIR spectral range, the total atmospheric water vapor and ozone contents are the main causes of atmospheric absorption.

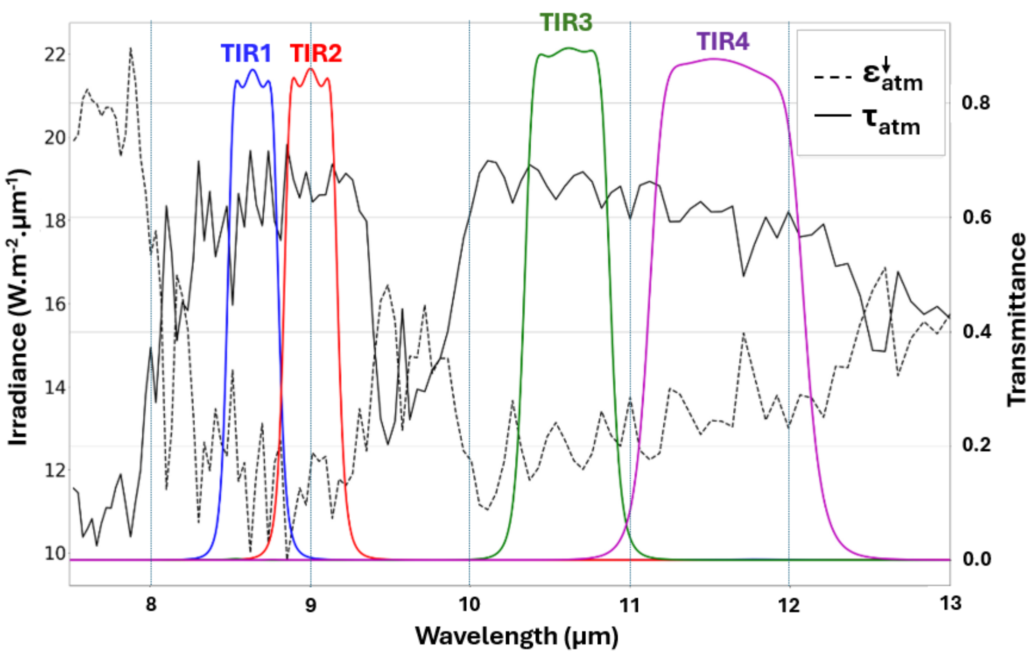

Figure 9 MODTRAN simulation of the TIR atmospheric transmittance spectrum

Figure 9 (adapted from Vidal et al., 2022) depicts the atmospheric transmittance spectrum (black line) in the 7.5 µm to 13 µm spectral range, obtained using MODTRAN6 computation over a representative selection of 24 atmospheric profiles of the

https://doi.org/10.5194/egusphere-2026-4492
Preprint. Discussion started: 31 July 2026

TIGR dataset (Chevallier et al., 2000). On the one hand, Fig. 9 shows no specific absorption feature for water over the whole spectral range considered, with transmittance lowering overall increasing atmospheric water, and vice versa. On the other hand, the spectrum show that two different atmospheric windows can be distinguished around 8-9.4 µm and around 10-12.5 µm, separated by the ozone absorption feature at 9.7 µm. Therefore, TIR bands for LST retrievals are located in those two atmospheric windows, as illustrated in Fig. 9 with the initial TRISHNA reference TIR spectral configuration. These wavelengths correspond to a maximum of thermal emission around 20°C, typical of Earth surface.

Consideration of surface emissivity is paramount in the positioning of TIR spectral bands, notably because the TIR signal is not only affected by the atmospheric absorption but also largely driven by the surface emissivity.

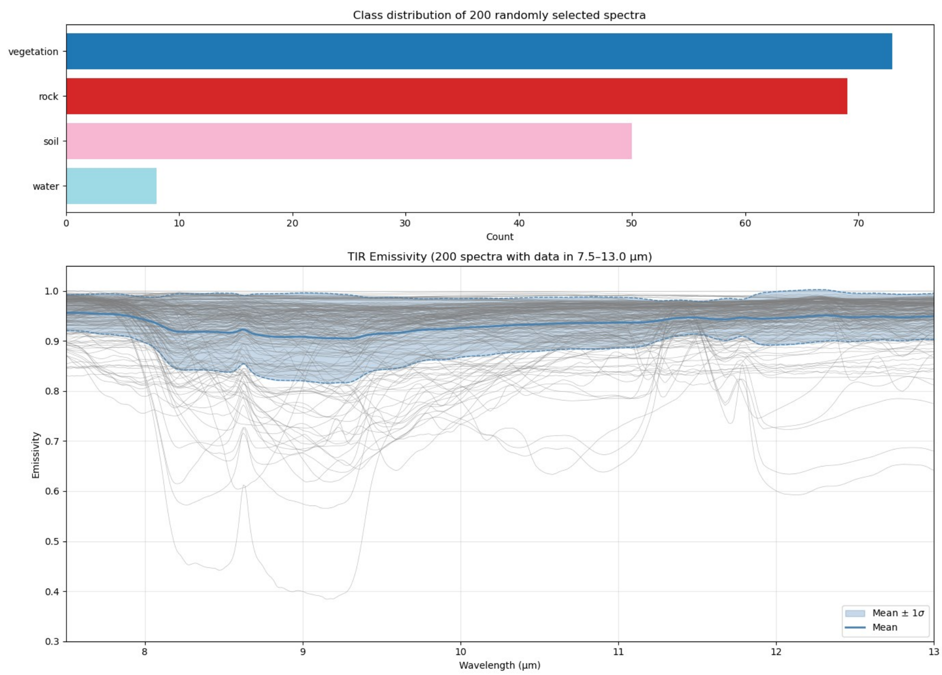

Figure 10 Emissivity spectra for 200 natural samples including rocks, soils, vegetation, and water. Average, average plus standard deviation, and average minus standard deviation spectra are also plotted (blue straight and dotted line)

Figure 10 displays the emissivity spectra for 200 natural samples including rocks, soils, vegetation, and water. The average, average plus standard deviation, and average minus standard deviation spectra are also plotted (blue straight and dotted line). It is clearly observed that emissivity values between 8 and 10 µm are lower due to Reststrahlen effect of minerals and show a higher variability than those values in the region between 10 and 13 µm. The higher atmospheric transmission in the 10-13 µm atmospheric window, jointly with the higher surface emissivity values and lower variability explains why typical TIR bands of existing remote sensing satellites (AVHRR, MODIS, AATSR, SEVIRI, etc.) for LST retrieval are allocated in that spectral region, provided that only one or two TIR bands are available. However, spectral bands in the atmospheric window in the 8-9.3 µm range can provide information on emissivity to obtain a better separation between LST and emissivity, notably spectral contrast, since that spectral range account for the main variance in emissivity. This principle is used in the Temperature and Emissivity Separation (TES) algorithm developed for ASTER (Gillespie et al., 1998), which exploits the relationship

https://doi.org/10.5194/egusphere-2026-4492
Preprint. Discussion started: 31 July 2026

between spectral contrast and minimum emissivity for natural species, as well as in the DirectTES algorithm (Marcq et al, 2023), which seeks to minimize brightness temperature variations over the TIR bands available.

In the TIR domain, the radiometric performances are not expressed as a signal to noise ratio, but as a standard deviation of noise expressed in degrees, which is noted NEdT, expressed at instrument level. Instrumental noise must be considered when positioning TIR channels by accounting for both the intersection of band spectral response functions with the edges of available atmospheric windows and the cross-talk between bands. Indeed, bands located near the edges of atmospheric windows (e.g., around 7.5 µm or beyond 12 µm) experience lower photon flux and therefore higher NEdT (Rogalski, 2011). And in addition, spectral cross-talk reduces radiometric fidelity by introducing correlated noise between bands and creating systematic biases in differential retrievals (Gruson et al., 2020).
The last main aspect to consider is the LST retrieval method used for the mission. Indeed, some methods, such as TES or DirectTES expect proper application that atmospheric effects are minimized overall, and that spectral contrast is maximized over the bands considered, while the Split-Window (SW) type methods expect atmospheric effects to be maximized locally, and spectral contrast minimized.

TRISHNA TIR bands selection

Prior to TRISHNA, the TIR band configuration proposed for MISTIGRI mission included 3 bands (TIR1 and TIR2 located in the 10-12.5 µm region and TIR3 located in the 8-9.3 µm region). There was an option to split the 1-µm-wide TIR3 band into 2 thinner spectral bands in order to better characterize emissivity, but a trade-off had to be made because of the increased noise of a narrow band (Jacob et al. 2021). Thanks to the reduced noise of the MCT-cooled detectors used for the TRISHNA mission as opposed to the MISTIGRI micro bolometers, the choice was made to use a 4 bands configuration with two bands in the 7.5 to 9.7 µm range (TIR1 and TIR2), and two bands in the 10 to 13 µm range (TIR3 and TIR4).

Two sensitivity analyses have been conducted for the optimization of the positioning of the TRISHNA TIR spectral bands, considering a representative range of atmospheric configurations, atmospheric and instrumental noises, and pair-wise variations of the bands position : Vidal et al. (2021) investigated the optimal placement of the TIR3 and TIR4 bands as related to SW LST estimation, and Vidal et al. (2022) investigated the optimal placement of all the bands as related to TES LST estimation.
Overall, the study led to the following constraints on the TRISHNA spectral configuration:

- For TIR1, shifting toward higher wavelengths renders the spectral configuration more robust to position and to bandwidth uncertainties by reducing water absorption impact on the surface temperature estimation. Considering that, we chose to place TIR1 at 8.65 µm;
- For TIR2, shifting toward lower wavelengths limits the ozone absorption interference, especially regarding uncertainties on position/FHWM. The new TIR2 position is then chosen to be at 9.0 µm;
- For TIR3, the study revealed the necessity of a shift toward higher wavelengths in order to avoid ozone interferences on the surface temperature estimation. Moreover, Vidal et al. (2021) showed that for SW application, an optimal position of TIR3 existed at 10.6 µm;
- For TIR4, the studied revealed a limited sensitivity of the TES inversion results to its position, however suggesting that shifting toward lower wavelengths will improve inversion results by minimizing atmospheric effects. Additionally, Vidal et al. (2021) also revealed that a limited cross-talk between TIR3 and TIR4 will be kept to ensure satisfactory SW inversion. Hence, we chose to keep TIR4 at its reference position of 11.6 µm.

https://doi.org/10.5194/egusphere-2026-4492
Preprint. Discussion started: 31 July 2026

	TIR1	TIR2	TIR3	TIR4
λ_c (µm)	8.65 ± 0.10	9.00 ± 0.10	10.6 ± 0.15	11.6 ± 0.15
FWHM (µm)	0.35 ± 0.07	0.35 ± 0.07	0.7 ± 0.15	1.0 ± 0.15

Table 3 Specifications for the position and width of the TIR spectral bands

These constraints allowed us to specify the TRISHNA spectral configuration specified in Table 3. Compared to the MISTIGRI configuration, this new configuration does not improve the TES inversion results significantly. However, it allows a better estimation of the surface temperature using the SW method up to more than 0.5 K. More importantly, the new configuration was structurally defined to be more robust to uncertainties on actual bands position and FWHM.

3.3.3 Definition of VNIR Spectral bands

Vegetation variables and albedo

For different bio-geophysical variables such as Leaf Area Index computation, vegetation indices, albedo, fractional vegetation cover and generation of level 2B product: 2 bands are necessary, in the red and NIR region.

For cloud detection

Cloud detection using only TIR data assumes that clouds are much cooler than the Earth surface. However, this is not true for all clouds (low altitude clouds, very thin clouds). This makes such algorithms difficult to tune: the detection threshold depends on the scene, and ancillary data are needed. Images with large and sharp contrasts in LST cause difficulties (water bodies and forests are cooler than bare soil, mountains are cooler than plains, wet areas are cooler than dry areas). Consequently, margins on the thresholds are considered, in order to avoid false detections, and some clouds remain inevitably missed.
Without VNIR bands, many clouds (thin or low clouds) would be missed, and a very large noise is expected in temperature time series. For that reason, TRISHNA data would not be reliable.

Very efficient algorithms exist (Hagolle et al., 2010), combining VNIR and TIR and multi-temporal imagery, taking advantage of the following properties: firstly, clouds are generally brighter and whiter than Earth surface, and secondly, clouds are mobile and cloud-top reflectance features are dynamic, while surface reflectance variations are generally slower.
VNIR bands (blue, red, NIR) are necessary, in combination with information from TIR. In addition, a SWIR band at 1.38µm will improve thin cirrus cloud detection.

A green band is desirable for water color information (estimation of chlorophyll and sediments concentrations) in combination with blue band, and to enhance spectral knowledge of the surface albedo. The Blue band is also required for AOD estimation.

Need for a water vapor band

We conducted a dedicated assessment that demonstrates that the use of ECMWF data for total water vapor retrieval does not achieve the level of accuracy required for a large number of use cases targeted by TRISHNA. The results highlight the interest of a Sentinel2-type water vapor channel (0.940 µm) for Atmospheric Water Vapor Content (AWVC) estimation, because the high spatial resolution data permit to better reproduce the realistic AWVC variations over heterogenous scenes, as opposed to the lower spatial resolution offered by the ECMWF data, including some flaws in the climate model. This outcome is

https://doi.org/10.5194/egusphere-2026-4492
Preprint. Discussion started: 31 July 2026

particularly true when considering area with high variations in surface elevation and vegetation density, which can both cause local abrupt variations of AWVC.

Moreover, as far as humid regions are concerned, the precision of AWVC estimate is expected to increase with a « water vapor channel » at 0.910 µm instead of 0.940 µm. We performed a study to demonstrate that 0.910 µm is the best option. Three main reasons were foreseen:

(i) First, a spectral band centered on 0.910 µm is closer to the NIR reference band (0.860 µm) used in the water vapor content retrieval algorithm. Thus, a lower error will be made in modeling the reflectance difference between the two bands. It shall be noted that, in the simple algorithm used for S2, the reflectance is assumed to be the same in the two channels, which let further room for improvement.

(ii) Second, the absorption by water vapor is nearly total at 0.940 µm for very humid regions. This makes water vapor retrieval difficult in these conditions. Conversely, while a 0.910 µm channel is still sensitive to the AWVC, the absorption is lower, thus enabling the algorithm to still deliver results. Results from the study show that for AWVC > 1 g/cm², the transmission in the 0.910 µm channel is overall 40% higher than in the 0.940 µm channel.

(iii) And third, as the silicon sensitivity largely decreases in the 900nm-1000nm range, a better sensitivity could be expected at 910 nm rather than 940 nm.

Our study shows that the error margin on AWVC allowed to correctly recover surface temperature decreases drastically with increasing AWVC, going from 0.9 g/cm² for AWVC < 2 g/cm² down to 0.1 g/cm² for AWVC around 6 g/cm². On the contrary, high error values on surface temperatures are expected when using ECMWF data, notably on the several problematic areas highlighted in the ECMWF/S2 comparison.

3.3.4 Choice of SWIR spectral bands

Retrieval of accurate aerosol optical depth is essential for incident solar flux and thereby net radiation. In TRISHNA mission, the blue and red band combinations can also be used to retrieve good aerosol optical depth through inversion instead of the SWIR band at 2.1µm. The SWIR band 1.6µm is indicated as mandatory for land surface albedo estimation and therefore net radiation and evapotranspiration. It is also used in the algorithms retrieving vegetation variables (Weiss and Baret 2016). Moreover, the 1.6 µm band will have substantially higher SNR due to higher albedo as compared to lower SNR at 2.1 µm. In addition, retrieval accuracy of AOD from 2.1 µm was found to be marginally higher as compared to that from 1.6 µm. Keeping in view of all these results and trade-off, in TRISHNA mission, the SWIR band at 1.6 µm is chosen.

A SWIR band centered at 1.38 µm is specifically used for cirrus cloud detection. This wavelength coincides with a strong atmospheric water vapor absorption feature (Gao et al. 1995), where absorption is sufficient to eliminate nearly all surface-reflected radiance below about 2000 m altitude, while still allowing signals from high-altitude clouds to be observed. By applying a simple threshold that accounts for ground elevation (Hagolle et al. 2017), it becomes possible to accurately detect high-level clouds, including thin cirrus that are otherwise difficult to identify (Baetens et al. 2019).

3.3.5 TIR Radiometric performance considerations

The Noise Equivalent Difference Surface Temperature, expressed at Earth surface level, is noted NEdTs. The impact of LST estimation error on the retrieval performance varies a lot according to the retrieval method. It is significant for a NEdTs greater than 2 K for instantaneous retrieval, but much less for assimilation of LST, and even less for assimilation of inverted soil moisture proxy.

Crow et al., 2008 studied the impact of LST measurement error on the performance of the root zone soil moisture retrieval when the latter is either extracted from LST instantaneously (θTSMrz) or when the soil moisture proxy is assimilated in a

https://doi.org/10.5194/egusphere-2026-4492
Preprint. Discussion started: 31 July 2026

model (WEB-SVAT/EnKF) named WEB-SVAT. From this study, we can conclude that even with the simplest assimilation, a significant improvement is obtained with NEdTs < 1.5 K.

Many factors contribute to the NEdT at the surface, including intrinsic sensor performance, uncertainties associated with radiometric calibration, atmospheric correction, the separation of surface emissivity from temperature, and directional anisotropy effects. Even if all these effects were perfectly known and corrected, atmospheric turbulence within the surface layer and the planetary boundary layer would still induce rapid temporal fluctuations in the observed surface temperature, resulting in typical error at the surface ranging from 1 to 1.5 K. These fluctuations were analysed by Lagouarde et al., 2013 with images acquired on different land surfaces in the South-West of France. It is still to be confirmed whether or not this phenomenon is of the same amplitude over water (rivers, coastal ocean, inland water bodies).
The NEdT requirement at instrument level for TRISHNA is set to 0.25 K at a temperature of 300 K for TIR1 and TIR2 spectral bands, and 0.2 K for TIR3 and TIR4. This requirement is consistent with an objective of a NEdTs of 1 K (as shown by Gillespie et al., 1998). Moreover, the Split Window method for estimating surface temperature can provide accurate LST with a NEdT=0.5 K, except in very humid tropical atmospheric conditions.
In addition to radiometric noise, the absolute radiometric calibration must be sufficiently accurate to avoid introducing a systematic bias in the retrieved land surface temperature. Therefore, the absolute calibration accuracy is specified to be better than 0.5 K (at 300 K), ensuring that calibration errors remain smaller than the random uncertainty associated with the instrument noise and do not become a dominant contribution to the overall LST error budget.

3.3.6 VNIR-SWIR radiometric considerations

Equivalent wavelengths are defined for each spectral band as the weighted average of the spectral response function, with the green band centered at 555 nm, the red band at 670 nm, and the NIR band set to 860 nm with a 40 nm bandwidth. A cirrus band (1380 nm) and a 1610 nm SWIR band are also included in the configuration.

For radiance computations, Thuillier et al. 2003 solar spectrum was used, with a simplified rectangular spectral response approximation applied across each band. The mission radiance range [Lmin, Lmax] was defined to ensure precise characterization of instrument linearity and equalization, with Lmin based on VENµS and LANDSAT-8/OLI requirements (Morfitt et al., 2015), Lmax computed for a surface reflectance of 1. The saturation radiance Lsat was set to 1.05 × Lmax to optimize dynamic range while accepting limited saturation under extreme conditions, e.g., bright clouds or snow. This reduced margin of 5% over Lmax is considered acceptable, assuming the instrument meets overall performance requirements.

SNR requirements are specified at Lmin for VNIR bands and at reference radiance (Sentinel-2) for SWIR bands, corresponding to a surface reflectance of ~0.05. Computations of top-of-atmosphere radiances under various atmospheric conditions (water vapor, ozone, aerosol optical thickness) were performed using the 6SV radiative transfer model.

For the cirrus band, surface reflectance assumptions differ because cirrus clouds exhibit much lower reflectance (~0.4) in the 1.38 µm band compared to water surfaces (Gao and Kaufman 1995).

The values can be cross-checked with histograms from Sentinel-2. They exhibit a sufficient margin w.r.t. the 99.9% histograms.

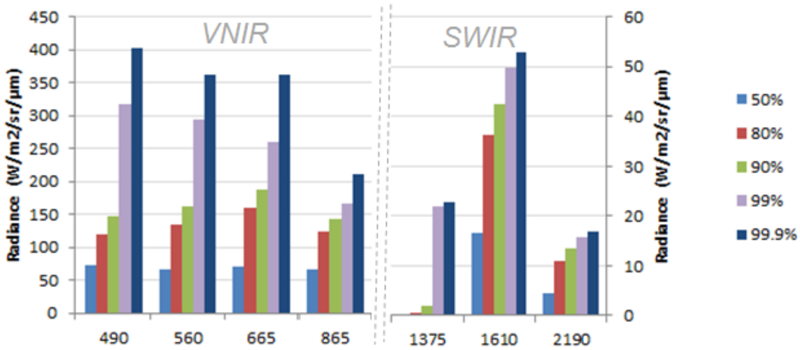

Figure 11 Sentinel-2 B histograms

The principle adopted for setting the radiometric requirements is that the total noise shall be shared in equivalent proportions between electronic noise and other sources (straylight, thermal stability, filters rejection and others).
The required performances are consistent with those for Sentinel2 (Drusch et al. 2012) and LANDSAT8 (Markham et al. 2014).

3.4 Geometric Requirements

In order to enable accurate use of time series of thermal infrared images, it will be necessary to achieve multi-temporal registration of images better than 0.9 pixel (CE99.7%, 3 sigma).
Such a performance cannot be achieved using orbit and attitude data alone, but requires an automatic geometric refinement during ground processing based on Ground Control Points (GCPs). These GCPs are automatically extracted by image correlation using the operational algorithms developed by CNES for the Pléiades mission (Lebègue et al., 2015). The GCP will be obtained with the VNIR bands, and used to enhance the geometric sensor model (attitude data mainly), and thus will be transferred to the TIR bands.

3.5 Retained TRISHNA configuration

3.5.1 Orbit and orbit-related parameters

The parameters relative to the orbit are given in Table 4 and Table 5. The average revisit time is shown in Fig. 12.

Parameter	Value
Orbit type	Sun-synchronous, phased
Phased orbit parameters Number of revolutions per day = n + p/q	(n,p,q) = (14,3,8)
Local Time of Descending Node	12:30 PM
Repeat cycle (q)	8 days
Altitude	761 km

https://doi.org/10.5194/egusphere-2026-4492
Preprint. Discussion started: 31 July 2026

Inclination	98.2 deg
Longitude of Ascending Node of Track 1	92.76154 deg W

Table 4 TRISHNA orbit parameters

865 **3.5.2 Swath, angles, Ground resolution**

Parameter	Value
Ground Sampling Distance (nadir to edge of scan)	57 m to 91 m (across-track)
Total Swath	1026 km
Maximum Sensor Zenith Angle (measured at the instrument)	34 deg
Maximum Observation Zenith Angle (OZA) (measured at the surface target)	38 deg
Mean revisit time at Equator (different view angles)	2.66 days

Table 5 TRISHNA GSD and angles

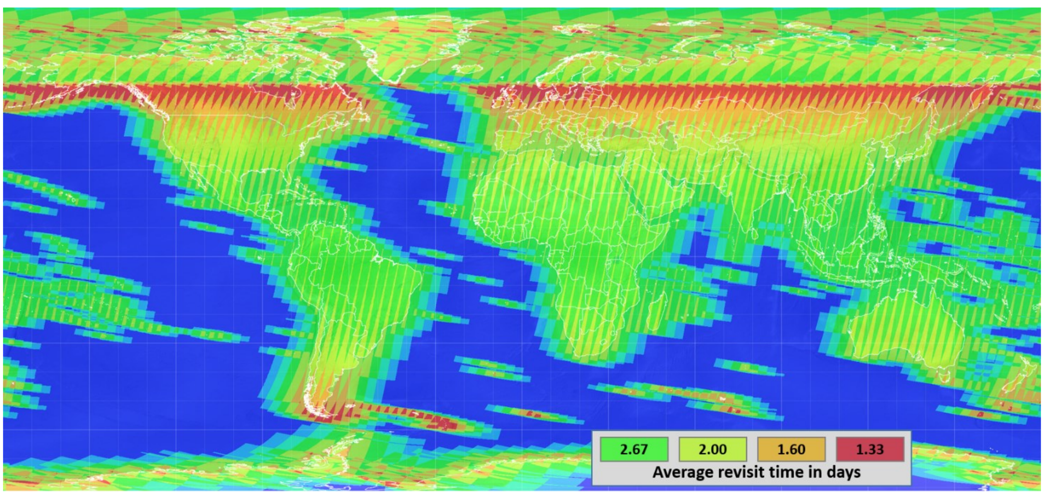

870 **Figure 12** TRISHNA average revisit time map

https://doi.org/10.5194/egusphere-2026-4492
Preprint. Discussion started: 31 July 2026

3.5.3 Acquisition scenario

The acquisition mask (Fig. 13 and Fig. 14) is defined to ensure full resolution coverage of all continental surfaces, including at least 100km from the coast, and up to 150-200 km from the coast in the Indian ocean, especially off the Somalian Coast, and Bay of Bengal (major rivers deltas). It also includes closed seas, the Mediterranean Sea, and Antarctica coastline.

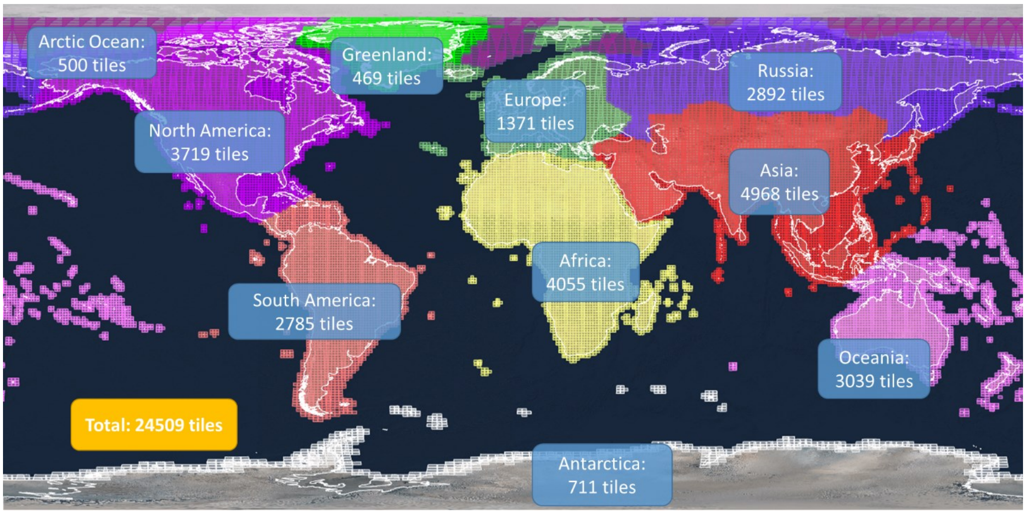

Figure 13 TRISHNA acquisition mask, with the number of Sentinel2 tiles per area

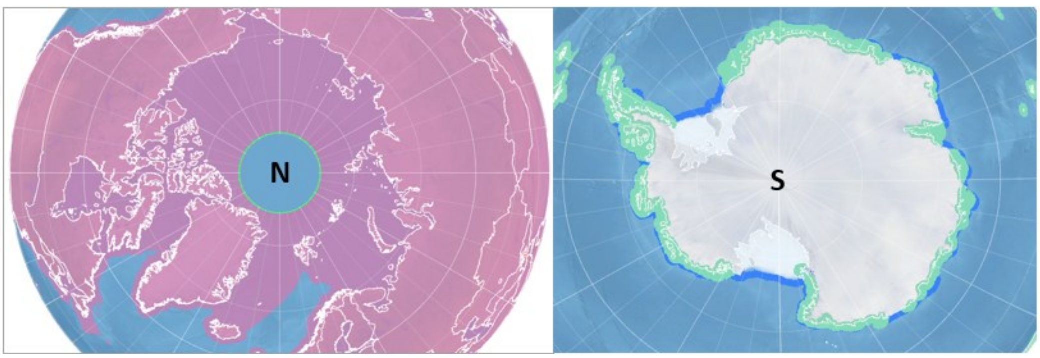

Figure 14 Acquisition mask on Arctic Ocean, exhibiting the 84.6°N UTM limit (left), and on Antarctica coastline (right)

3.5.4 Spectral bands

The specified central wavelengths, bandwidths and radiometric requirements are summarized in Table 6 and Table 7.

Band name	Wavelength Center (nm)	FWHM (nm)	L_{min} (W/m^2/sr/µm)	L_{max} (W/m^2/sr/µm)	SNR @ L_{typ}
Blue	485	70	30	663.5	50
Green	555	70	30	600.5	100
Red	670	60	20	486.1	100

https://doi.org/10.5194/egusphere-2026-4492
Preprint. Discussion started: 31 July 2026

NIR	860	40	30	325.3	100
WV	910	30	30	277	50
Cirrus	1380	30	6	55.0	25
SWIR	1610	100	4	77.9	100

Table 6 VSWIR central wavelengths, bandwidths and radiometric requirements

Band name	Wavelength Center (µm)	FWHM (µm)	NEdT @300K (K)	$T_{saturation}$ (K)
TIR 1	8.65	0.35	0.25	> 350
TIR 2	9.0	0.35	0.25	> 350
TIR 3	10.6	0.7	0.2	> 350
TIR 4	11.6	1.0	0.2	> 350

Table 7 TIR central wavelengths, bandwidths and radiometric requirements. Note that the saturation temperature is expressed as top-of-atmosphere brightness temperature

4 System definition

4.1 Overview

The major components of the TRISHNA System are:

- The Control Ground Segment includes a command-and-control center, in charge of the satellite command and control functions including TIR commanding and VNIR/SWIR mission scheduling.
- The satellite, which is composed of two payloads, the TIR and the VSWIR instrument, as described above, and of a bus.
- The CNES and ISRO X band earth terminals and their connection to the payload ground segments are used for the downloading and the routing of the science data toward the Payload Ground Segments.
- Two payload ground segments with the same capabilities are implemented, one in India (NRSC-Shadnagar, Hyderabad), one in France (CNES, Toulouse).

4.2 Flight segment

4.2.1 Bus

The TRISHNA satellite is based on the IRS-1K heritage platform developed by ISRO, with specific adaptations to the payload deck. This platform builds upon a well-established family of ISRO Earth observation satellite buses, whose performance and design have been validated through numerous missions, including early IRS series satellites (e.g., IRS-1A mission) and the joint Megha-Tropiques mission carried out in cooperation with CNES.

The platform has a dry mass of 770 kg, within a total satellite capacity of 1220 kg. Its power subsystem delivers up to 2 kW, relying on two nickel–cadmium batteries to ensure continuity of operations during eclipse periods. The satellite operates in a Sun-synchronous orbit and is three-axis stabilized, achieving a pointing accuracy of 0.1° in pitch, roll, and yaw. This level of performance is ensured by a zero-momentum reaction wheel system, combined with Earth, Sun, and star sensors, as well as gyroscopic measurements for precise attitude determination.

https://doi.org/10.5194/egusphere-2026-4492
Preprint. Discussion started: 31 July 2026

The platform provides a range of services to the payloads, including time-tagged commanding capabilities that enhance operational flexibility. It also incorporates a mass memory capacity of 1.4 Tbits and an X-band downlink enabling data transmission at rates up to 960 Mbps. A 50 kg propellant tank is allocated to support orbit acquisition and maintenance over a nominal mission lifetime of seven years.

The satellite carries two instruments: a thermal infrared (TIR) instrument and a visible to shortwave infrared (VSWIR) instrument.

4.2.2 Characteristics of the Thermal Infrared instrument

The TIR instrument (Fig. 15) is developed by CNES with Airbus as prime contractor, as described in Charvet et al., 2022. The main TIR requirements are summed up hereafter:

The key features are:

- Scan mechanism allowing to address the +/-34° swath and calibration targets at each acquisition cycle
- Instrument entrance pupil equivalent diameter 150 mm
- Internal blackbody and cold space view for radiometric calibration
- Full AlSi TMA telescope and optical bench
- Telecentric optical design
- Focal plane cooled down to 60 K including an MCT detector (PEGA from LYNRED) and 4 spectral filters
- Cryostat structure in Additive Layer Manufacturing technology
- Two LPT6510 cryocoolers from TCBV, operated in hot redundancy

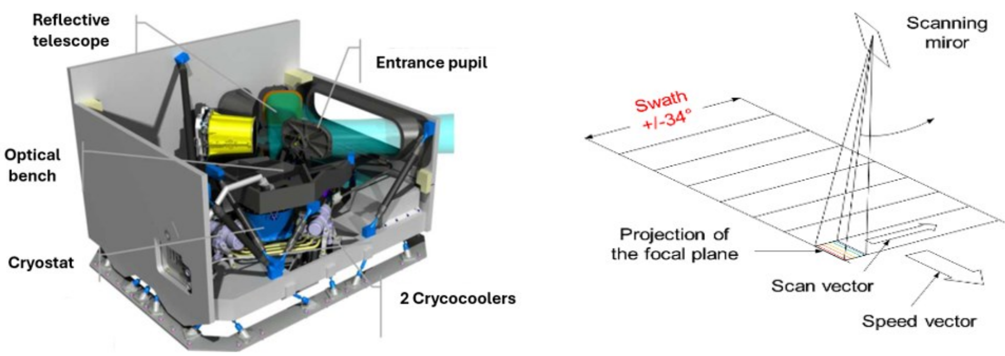

Figure 15 TIR instrument overview (left) and acquisition principle (right), adapted from Charvet et al., 2022

The TIR instrument design is an optimal combination of recurring elements and innovative features which allow to achieve the required performance.

4.2.3 Characteristics of the VNIR/SWIR instrument

https://doi.org/10.5194/egusphere-2026-4492
Preprint. Discussion started: 31 July 2026

Developed by ISRO, this instrument (Fig. 16) includes 7 spectral bands. The total mass is 120 kg. The VSWIR is a pushbroom concept (line acquisition with satellite displacement):

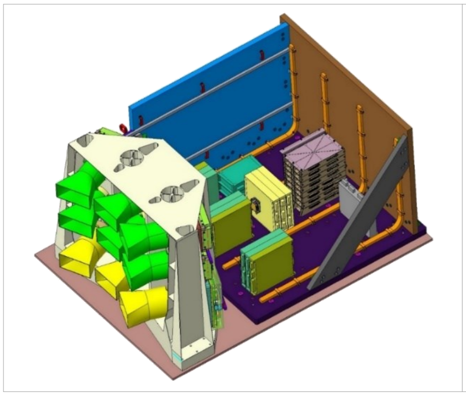

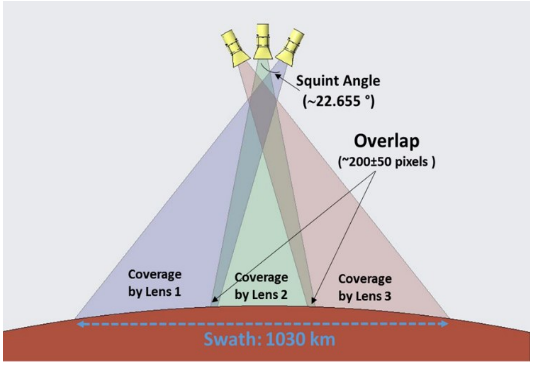

Figure 16 Scheme of the VSWIR instrument (left) and swath coverage (right) (Courtesty of ISRO)

The instrument concept relies on a multi-head optical architecture designed to achieve a wide field of view of ±34°. This total swath is distributed among three optical heads, each covering a portion of the across-track field. Each head integrates three co-aligned cameras dedicated to distinct spectral domains: one in the visible and near-infrared (5 VNIR bands), one for the cirrus band, and one for the 1.6µm shortwave infrared band. This architectural choice is driven by the objective of leveraging existing, flight-proven filter and detector assemblies.

4.3 Mission Ground Segment

4.3.1 Two Payload Ground Segments

As mentioned previously, there are two Payload Ground Segments.

ISRO (respectively CNES) is in charge of the development, the validation, the exploitation and maintenance of the Indian (respectively French) Payload Ground Segment.

Each payload ground segment is composed of 5 different components:

- A payload data server (PLDS), in charge of receiving and distributing all files in interface with PLGS external entities
- A payload data processing ground segment (PLDP), in charge of building up the products from level 0 to level 3
- A Technical expertise center (TEC), one at CNES for the TIR instrument, one at ISRO for the VNIR/SWIR instrument, which encompasses the payload expertise function in charge of instrument calibration and characterization and a products expertise function in charge of quality monitoring and algorithm expertise.
- A data distribution which distributes the products to the scientific community

In addition, the French ground segment will implement a Payload Operation Center (PLOC) for TIR instrument command and control and technological operations management (vicarious calibration).

4.3.2 Data production and dissemination, latency and archive:

As a demonstration of the mission potential in real-time irrigation management, the goal is to distribute the products 12 hours after their acquisition.

Since the global production represents a huge amount of data, the worldwide production and data storage is shared by the two ground segments. There is no duplication of the production nor storage (except for selected cross-validation sites).

https://doi.org/10.5194/egusphere-2026-4492
Preprint. Discussion started: 31 July 2026

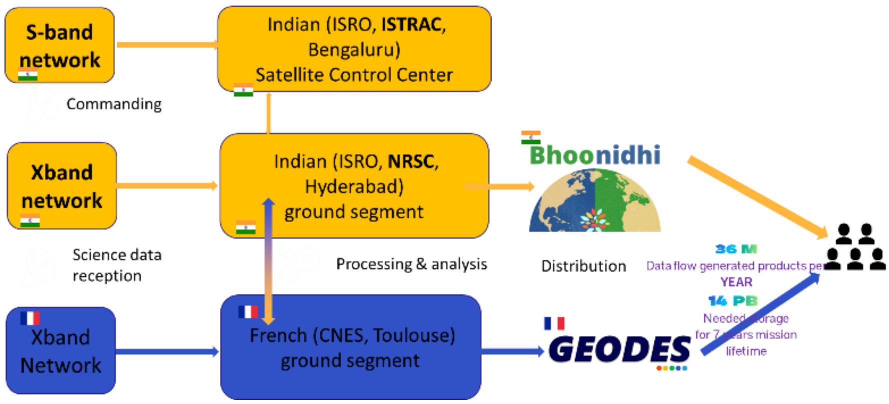

Figure 17 Mission data collection, processing and distribution

Any data will be accessed from both portals Bhoonidhi (National Remote Sensing Centre (NRSC), *Bhoonidhi – ISRO Earth Observation Data Hub* https://bhoonidhi.nrsc.gov.in) and GEODES (Centre National d'Études Spatiales, *GEODES – Earth Observation spatial data portal* https://geodes.cnes.fr), as shown in Fig. 17.

Level 0, 1A, 1B products are for internal use only. They are not distributed to the users.
Level 1C, 2A, 2B and 3 products will be distributed to the users, according to the TRISHNA open data policy.

5 Overview of the products and calibration/validation strategy

5.1 Processing chain

The TRISHNA processing chain (Levels 0 to 3) is presented in Fig. 18. At Levels 0 and 1, the received telemetry is first sorted chronologically, and initial geometric models are established (GEO-INIT). Radiometric and spectral artefacts are then corrected, followed by absolute calibration and conversion to radiance (RADIO). The images are subsequently co-registered with reference data (GEO-REFINE) and resampled onto a UTM grid consistent with Sentinel-2 tiling, where the geometric correction is applied (GEO-PROJ).

At Level 2A, surface radiative variables are retrieved through atmospheric correction and temperature-emissivity separation (ATMO-CORR). This step is followed by the estimation of vegetation biophysical variables (VARBIO), as well as albedo and surface fluxes. Level 3 products are finally derived as continuous time series (GAP-FILLING).

https://doi.org/10.5194/egusphere-2026-4492
Preprint. Discussion started: 31 July 2026

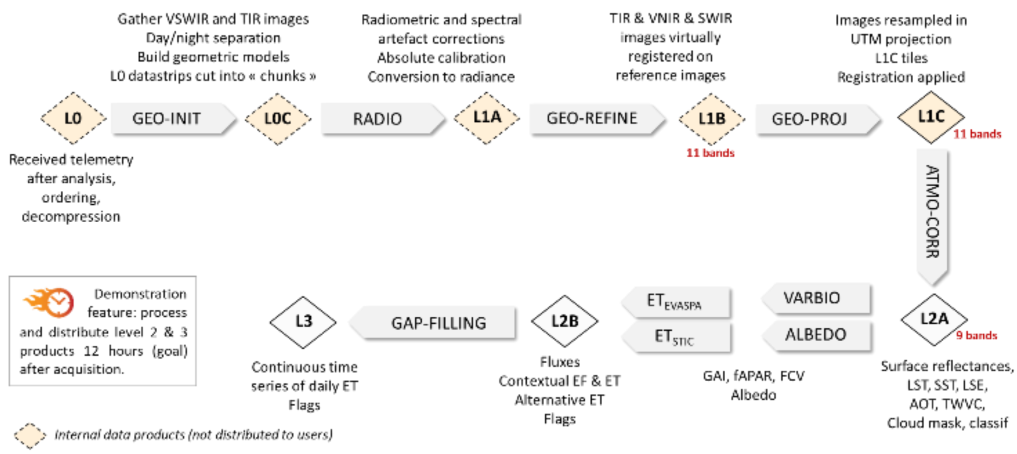

Figure 18 Products processing chain overview

5.2 Products

5.2.1 Level 0 and 1 Products

Level 0 product is a raw data product, according to the CEOS definition. It corresponds to a complete decompressed image data-strip from one of the instruments, with full swath. It contains 7 spectral bands for the VSWIR L0 product, and 4 spectral bands for the TIR L0 product. It contains raw data after restoration of the chronological data sequence at full time and spatial resolution. It includes all auxiliary and ancillary information to be used in subsequent processing.

Level 1A products are generated from the extraction of single-resolution data from level 0 products of a given instrument. The Level 1A Product contains radiometrically normalized data from one of the instruments after decompression, selection of the part of the swath relative to the requested resolution, and 'scene' extraction; a scene is a subset along the data strip with all spectral bands of the camera. The scene size is limited by the source data strip. Bands are coarsely registered.

Level 1B products are generated from level 1A products of a given instrument. The level 1B product provides geo tagged digital counts after radiometric correction, for a scene, in the focal plane geometry. Bands are coarsely registered.

Level 1C products are built from the gathering of VSWIR level 1B products and TIR level 1B product. Exogenous information is also used (mainly reference grid and DEM). The level 1C Product provides georeferenced TOA radiative variables: TOA reflectances for VSWIR channels, TOA brightness temperature for TIR channels.

5.2.2 Level 2A Products

Level 2A products are generated from 1C products. Data from both instruments can be used to generate level 2A products. Exogenous information (mainly meteorological data) will be also used as input. To allow multi-temporal methods or to process data acquired by night, previous L2A are used as input.

Level 2A products provide reflectances, emissivities and temperatures at surface level, as well as aerosol optical depth and total atmospheric water vapor content. Dedicated algorithms are activated, depending on whether the surface is water or land and acquired by day or by night.

https://doi.org/10.5194/egusphere-2026-4492
Preprint. Discussion started: 31 July 2026

VSWIR data is only acquired during daytime. Over land, VSWIR instrument data is processed by MAJA (Hagolle et al., 2017, available on https://github.com/CNES/MAJA). To retrieve the integrated water vapor content, cloud mask, aerosol optical thickness and calculate surface reflectances, using a combination of multi-temporal and multi-spectral criteria Over water, the reflectances (dimensionless, fully-normalized for sun and sensor at nadir) are calculated using POLYMER atmospheric correction (Steinmetz et al., 2011), which is able to recover water color in the presence of sun glint.

The TIR instrument data is processed both daytime and nighttime. A specific night cloud mask using only TIR data with DEM information, based on the Bayesian theory is inspired from Hollstein et al., 2015. Over land, meteorological data from the ECMWF (e.g. water vapor and temperature profiles) is scaled to TRISHNA resolution, taking into account the water vapor content retrieved from the VSWIR data processing and fed to the RTTOV radiative transfer code (Matricardi et al. 2001; Saunders et al., 1999) to compute atmospheric correction parameters (transmittance, upwelling and downwelling radiance). The temperature and emissivity separation is then performed using direcTES (Marcq et al, 2023). Over water, surface temperature is calculated with the split window based NLSST algorithm (Walton et al 1998).

5.2.3 Level 2B Products

Vegetation variables

TRISHNA's spectral sampling provides enhanced information on canopy structure and optical properties compared to classical vegetation index approaches, enabling more constrained and robust retrievals. The distributed vegetation variables are:

- GAI (Green Area Index): total green leaf area per unit ground area (m^2/m^2), reflecting canopy density. It is sensitive to canopy structure and seasonal growth.
- Fcover (Fractional Vegetation Cover): fraction of ground covered by vegetation from a top view. It measures horizontal coverage, ranging from 0 (bare soil) to 1 (full canopy cover). Fcover does not account for vertical leaf layering: two canopies with same Fcover can have different GAI.
- FAPAR (Fraction of Absorbed PAR): fraction of incoming photosynthetically active radiation (400-700nm) absorbed by the canopy. It measures light absorption and photosynthetic activity, so it is directly linked to primary productivity and carbon assimilation. A high fAPAR implies efficient absorption of light, whereas a low value indicates sparse or stressed vegetation.

State-of-the-art reviews indicate that machine learning approaches provide the best performance for biophysical variable retrieval, as they efficiently handle nonlinear processes and offer high computational efficiency (Smith, 1993; Weiss et al., 2002; Bacour et al., 2006; Duveiller et al., 2011; Weiss and Baret 2016). Among these methods, neural networks and Gaussian processes show comparable accuracy when trained on similar datasets. Neural networks were selected for TRISHNA due to their computational efficiency and proven performance in operational algorithms, such as the Sentinel-2 SNAP vegetation products.

To ensure global applicability, the algorithm relies exclusively on instantaneous TRISHNA observations and does not use auxiliary data, despite the inherently ill-posed nature of the inversion problem. This generic approach ensures robustness across diverse vegetation types, though it may be less accurate than surface-specific algorithms for certain variables, particularly GAI. The training database is generated using radiative transfer model simulations to represent the full range of vegetation types, conditions, and reflectance uncertainties observable by TRISHNA. Particular attention is given to realistic leaf optical properties and background reflectance variability.

Product quality is ensured through multiple indicators, including propagation of input reflectance quality flags, a unified product confidence flag based on land cover consistency with model assumptions, range validity checks, and quantitative uncertainty estimates provided by the algorithm.

https://doi.org/10.5194/egusphere-2026-4492
Preprint. Discussion started: 31 July 2026

Albedo

Albedo retrievals can follow two approaches: a modular processor chaining directional normalization, spectral computation, and narrow-to-broadband conversion, or a more physically rigorous inversion of the coupled surface–atmosphere radiative transfer problem (Pinty et al., 2000; Govaerts et al., 2008; Liang, 2003). The modular approach, balancing accuracy, efficiency, and operational robustness, has been adopted for near-real-time products from POLDER, MODIS, SEVIRI, and within the LSA-SAF framework (Strahler et al., 1999; Geiger et al., 2008; Carrer et al., 2010). Since 2013, operational products from the Copernicus Global Land Service, now based on PROBA-V and Sentinel-3 (Roujean et al., 2018), represent the current European state of the art and serve as the basis for TRISHNA.

Evapotranspiration

Thermal infrared-based evapotranspiration models exploit land surface temperature as a proxy for the integrated outcome of the complex biophysical processes governing ET, stomatal regulation, plant hydraulic conductance, root water extraction, and vapour transfer at the soil surface, without explicitly resolving any of them. This substitution is physically justified because LST responds directly and measurably to the partitioning of available energy between sensible and latent heat, making it a powerful integrative observable of surface water status. Although the theoretical foundations of LST-based ET retrieval are well established (Lagouarde and Boulet, 2016), the primary sources of uncertainty in operational implementations are not the retrieval equations themselves but the accuracy and spatial representation of the ancillary inputs. These include air temperature, downwelling radiation, wind speed, and aerodynamic parameters. When extending instantaneous latent heat flux estimates to daily ET, an additional and often substantial source of uncertainty arises from the temporal extrapolation and the quality of the meteorological variables used to support it, particularly daily downwelling solar radiation.

The practical difficulty of obtaining spatially representative meteorological data particularly air temperature and wind speed, and aerodynamic parameters such as roughness length and vegetation height at the native spatial resolution of TRISHNA (60 m) motivated the adoption of contextual approaches based on evaporative fraction as the primary ET estimation framework. Contextual methods avoid the need for spatially distributed meteorological forcing by exploiting the spatial variability of LST within a scene to infer the relative partitioning of available energy between sensible and latent heat. The method assumes that the atmospheric conditions are spatially homogeneous across the domain. The adopted framework for TRISHNA is the EVASPA tool (Gallego-Elvira et al., 2013; Olioso et al., 2016; Allies et al., 2020; Olioso et al., 2022), which provides continuous daily ET estimates through a multi-model, multi-data ensemble approach. The ensemble formulation additionally yields explicit uncertainty estimates for each ET retrieval, a capability rarely available in single-model operational frameworks. The validity of contextual methods rests on three core assumptions, (1) spatial variations in LST within the scene are driven exclusively by differences in surface water status, fractional vegetation cover, or surface albedo; (2) climate variables and aerodynamic parameters are spatially uniform; and (3) wet and dry pixel extremes representing the upper and lower bounds of evaporative demand are identifiable within the scene. Violations of these assumptions arising from mesoscale atmospheric heterogeneity, topographic variability, or the absence of fully wet or fully dry pixels represent the principal structural limitations of contextual approaches and must be carefully evaluated in landscapes with very homogeneous land use, or on the contrary for complex terrain or climatically heterogeneous landscapes.

When these conditions are not met, a flag is raised. In any case, an alternative product is proposed. It is provided by the surface energy balance model, STIC (Surface Temperature Initiated Closure) (Mallick et al. 2018, 2022). STIC is a one-dimensional (1D) analytical surface energy balance framework in which land surface temperature is directly integrated into the Penman-Monteith equation to solve for latent heat flux and its governing conductances. The model assumes vertical (1D) exchanges

https://doi.org/10.5194/egusphere-2026-4492
Preprint. Discussion started: 31 July 2026

between the land surface and the atmosphere and enforces closure of both energy and mass fluxes without relying on prescribed empirical parameterizations of surface roughness needed to solve aerodynamic conductance.

A central feature of STIC is the reformulation of the Penman-Monteith equation by explicitly incorporating LST to constrain the aerodynamic temperature and the vapor pressure deficit at the evaporating surface. This enables a fully coupled solution of sensible and latent heat fluxes. Instead of using prescribed function to characterize roughness lengths for determining aerodynamic conductance, STIC derives the “critical conductances” analytically by combining the energy balance equation with state equations linking LST, radiative flux components, air temperature, vapor pressure deficit, and vegetation spectral reflectances at VNIR and SWIR domains. Through this integration, LST serves as the key state variable that links radiative forcing to turbulent fluxes. The model simultaneously solves for aerodynamic conductance, surface conductance, sensible, and latent heat flux, ensuring internal consistency between energy partitioning and surface moisture constraints. This analytical closure reduces equifinality commonly found in widely used surface energy balance models, where conductances are often parameterized or externally prescribed. In its 1D formulation, STIC assumes homogeneous surface conditions within a pixel and neglects horizontal advection. Within these assumptions, it provides a physically consistent framework to retrieve ET and stomatal behavior directly from satellite-derived LST and standard meteorological inputs, making it particularly suitable for high-resolution remote sensing applications. Comparison of STIC with several other models over a large dataset of ECOSTRESS images showed lower errors (Hu et al. 2023). However, under severe aridity, STIC also showed systematic overestimation. This is due to a key limitation of 1D surface energy balance models (such as STIC) that they assume purely vertical exchanges, neglecting horizontal processes like advection and spatial heterogeneity. In real landscapes, especially in semi-arid and heterogeneous systems, lateral exchanges of heat and moisture (e.g., from hot bare soil to cooler vegetated patches) strongly influence surface temperature and flux partitioning. These are inherently 2D processes, which are not explicitly resolved in a 1D framework. This is where the LST-SWIR-VNIR synergy as implemented in TRISHNA version of STIC becomes critical.

LST alone reflects the integrated energetic response of the surface. However, in a 1D model, similar LST values can arise from different physical conditions: true stomatal closure due to water stress, increased sensible heating due to advection, and exposure of hot soil in sparse canopies. Without additional constraints, this leads to equifinality, where different processes produce the same thermal signal. The inclusion of SWIR and VNIR information provides independent physical constraints that help compensate for the absence of explicit 2D processes. The LST-SWIR-VNIR combination acts as a proxy for missing lateral information. It helps identify heterogeneity within a pixel (e.g., mixed soil-vegetation signals), it constrains surface vs root-zone water control, and reduces bias in estimating stomatal conductance and ET. When integrated into a 1D model such as STIC, these additional constraints effectively mimic some of the information that would otherwise require a 2D representation, without increasing model complexity. In the context of TRISHNA, the simultaneous availability of high-resolution LST and SWIR-VNIR observations provides a unique opportunity to move beyond purely thermal approaches and partially bridge the gap between 1D process representation and real-world 2D surface heterogeneity.

5.2.4 Level 3 Products

The L3 product provides daily evapotranspiration (mm/day) time series, a value every day, to facilitate downstream applications in water resource and crop management (Guillevic et al. 2019).

This product is created from the L2B daily single pixel evapotranspiration and the L2B daily contextual evapotranspiration but also from external radiation data and from meteorological data for days without TRISHNA acquisition (Delogu et al. 2021, Farhani et al. 2022, Allies et al. 2022).

https://doi.org/10.5194/egusphere-2026-4492
Preprint. Discussion started: 31 July 2026

Concretely, level 3 processing reconstructs a complete daily ET time series using gap-filling methodologies. For each pixel, a daily ET value is either directly taken from a valid Level 2 observation or computed via interpolation between adjacent valid dates, or extrapolation from previous observations when no Level 2 data are available.

A sliding window of several days (typically one week) allows the product to be continuously updated as new clear-sky acquisitions become available. Once a date moves outside the sliding window, the daily ET value is archived and no longer updated. Interpolated values are refined when new observations are added, while high-quality Level 2 ET values remain unchanged.

The Level 3 product generates two complementary ET time series: contextual daily ET from the EVASPA algorithm and single-pixel daily ET from the STIC algorithm. Interpolation between acquisitions uses progressively more sophisticated methods in successive iterations, and in cases of large gaps, backward extrapolation may be applied to improve reconstruction: the simplest approach is linear interpolation, using incoming solar radiation as a support variable to improve temporal consistency. A more advanced method accounts for soil re-humectation due to precipitation, adjusting the ET values to reflect post-rainfall increases in available water. The most sophisticated approach integrates a full soil water balance model (e.g. Ollivier et al., 2021), combining energy and water fluxes to constrain the interpolated ET in accordance with underlying hydrological dynamics. This approach allows progressively more physically realistic reconstructions while balancing computational cost and data requirements.

5.3 TRISHNA distributed products

The variables in TRISHNA distributed products are listed in Table 8.

Level	Content	Variables
1C	Top-of-Atmosphere variables Radiometrically and geometrically calibrated Orthorectified and resampled on a uniform spatial grid (Sentinel-2 tiles, Copernicus DEM)	✓ TOA reflectances x7 VNIR/SWIR bands ✓ TOA brightness temperatures x4 LWIR bands ✓ Cloud mask
2A	Surface radiative variables	✓ Land & Water Surface reflectances x 5 VNIR/SWIR bands ✓ LST, SST ✓ LSE x4 LWIR bands ✓ Cloud mask, TWVC, AOT
2B	Ecosystem variables	✓ GAI, FCOVER, fAPAR ✓ Albedo ✓ Downward solar flux

https://doi.org/10.5194/egusphere-2026-4492
Preprint. Discussion started: 31 July 2026

		✓ Daily evapotranspiration (contextual) ✓ Daily evapotranspiration (single-pixel) ✓ Water stress factor
3	Ready-to-use ecosystem stress and water use variables	✓ Continuous time series of daily evapotranspiration (contextual) ✓ Continuous time series of daily evapotranspiration (single-pixel)

Table 8 Distributed products

5.4 Overview of the calibration/validation strategy

TRISHNA CAL/VAL strategy combines statistical satellite-based methods, natural reference targets, permanent ground validation sites, and targeted field campaigns to ensure accurate radiometric calibration and reliable geophysical products throughout the mission lifetime.

Initial verification relies on in-orbit calibration using onboard references (TIR) and natural targets, complemented by inter-calibration with other satellite sensors and statistical analyses over stable surfaces such as deserts, oceans, and clouds. These approaches enable continuous monitoring of instrument performance and ensure the consistency of top-of-atmosphere reflectances and brightness temperatures (level 2A) throughout the mission lifetime.

A central component of the strategy is the use of existing ground-based validation networks and dedicated field campaigns to evaluate the accuracy of higher-level products, including surface reflectance, land surface temperature, emissivity, and atmospheric parameters.

The CAL/VAL strategy for Level-2B and Level-3 products of the TRISHNA mission focuses on validating higher-level biophysical and energy balance variables such as surface fluxes, evapotranspiration, vegetation variables, albedo, and downwelling radiative fluxes. Unlike Level-1 and Level-2A validations, which primarily assess radiometric performance and surface radiative variables, Level-2B/3 validation aims to evaluate how well TRISHNA products represent ecosystem processes and land–atmosphere interactions under real environmental conditions. This requires validation over representative landscapes and dynamic ecosystems, where surface properties, vegetation structure, and water availability vary in time and space.

To support this objective, the strategy relies on a network of instrumented “supersites” in India, in South of France and in Sahel, equipped with comprehensive in situ measurements of meteorological variables, radiation, surface temperature, soil moisture, and turbulent fluxes (e.g., eddy covariance). These supersites provide long-term, high-quality datasets that enable the validation of energy balance components and evapotranspiration estimates derived from TRISHNA observations across different climates, vegetation types, and hydrological conditions. Additional targeted field campaigns may complement these sites to address specific scientific questions, such as the effects of surface heterogeneity, canopy structure, atmospheric turbulence, or snow emissivity.

https://doi.org/10.5194/egusphere-2026-4492
Preprint. Discussion started: 31 July 2026

6 Synergies with other Earth Observation missions

Like TRISHNA, the following future missions plan to provide global sub-weekly estimates during the afternoon:

LSTM, ESA's COPERNICUS High Priority Candidate mission for land surface temperature, will improve the temporal (2 days) and spatial (35 to 50 meters) resolutions of TRISHNA, with 5 bands in LWIR.

EAGLE is a global hyperspectral VSWIR & multispectral TIR remote sensing NASA-JPL mission for ecosystems, mineralogy, coastal zone, natural hazards, snow & ice. The current mission design includes a 60-meter resolution, and a 3-day revisit.

The orbital configuration of TRISHNA and LSTM generates a structured and highly predictable spatiotemporal sampling pattern. Because the relative drift between the two satellites is governed by a fractional difference in orbital revolutions, their mutual overpasses (interferences) are evenly distributed in time and longitude once one crossing point is fixed. Over a period of approximately 2 + 2/3 days, TRISHNA completes 38 + 1/3 revolutions while LSTM completes 37 + 1/3, leading to three successive overtakes separated by 120° in argument of latitude. Consequently, these alignments occur at three distinct latitudes, providing latitudinal diversity in coincidence geometry. During certain phases of this cycle, TRISHNA becomes co-aligned with one LSTM platform, enabling high-quality intercomparison, cross-calibration, and radiometric harmonization without increasing instantaneous global coverage. In complementary phases, TRISHNA samples the longitudinal gaps between the two LSTM satellites, effectively densifying revisit frequency and enhancing temporal resolution. This resonance pattern repeats with strong similarity every ~2.67 days and achieves near-perfect recurrence every 8 days—corresponding to TRISHNA's repeat cycle—at which point TRISHNA has completed three additional orbits relative to a single LSTM.

Merging the sets of observations from these different missions would allow densified time series of LST, closer to the daily revisit, which is more appropriate to ET estimation. None of the foreseen missions can reach this goal individually. Moreover, multi-mission time series allows the diurnal ET cycle to be better constrained. While the 100 m resolution of Landsat 8/9 TIRS is a limitation for per-parcel estimation in many parts of the world (but this will be improved with LANDSAT-Next), over large parcels or homogenous areas, the diurnal signal could be retrieved. In addition, a strong synergy exists between thermal and optical missions that fly at similar local time. For example, some opportunities exist to downscale and interpolate Landsat 8 thermal observations using Sentinel-2 data through data fusion algorithms (eg. Yang et al., 2017; Semmens et al., 2016).

To ensure consistency, interoperability, and long-term performance alignment among TRISHNA, LSTM and EAGLE-TIR, there is overlap among the LSTM Mission Advisory Group, the TRISHNA Science Team, and the EAGLE-TIR Mission Science and Applications Team, with several experts contributing actively across all three bodies. The following coordinated actions are required:

First, mission strategies are coordinated, including harmonized overpass times and acquisition masks, in order to maximize simultaneous observations and enable systematic inter-comparison. Such coordination enhances the robustness of cross-mission analyses and strengthens the statistical basis for consistency assessments.

https://doi.org/10.5194/egusphere-2026-4492
Preprint. Discussion started: 31 July 2026

Second, product harmonization is essential to improve the comparability and interoperability of derived geophysical variables, with particular emphasis on performance alignment. This includes, to the greatest extent possible, the use of common—or at least performance-equivalent—auxiliary data sets (e.g., atmospheric profiles, emissivity databases, cloud masks, and geolocation inputs). Ensuring comparable input data and processing assumptions will facilitate convergence in retrieval performance and uncertainty characterization across missions.

Third, compatibility in product structure and formatting should be pursued to enable seamless integration of datasets into downstream applications. The objective is to allow users to ingest LSTM, EAGLE-TIR, and TRISHNA products without major format conversions or mission-specific adaptations, thereby reducing risks of processing errors and limiting additional costs related to development, validation, and long-term maintenance.

Furthermore, coordinated in-flight inter-comparison activities should be implemented to quantify radiometric consistency and retrieval biases under real observational conditions. These efforts should be supported by a common calibration and validation framework, including harmonized protocols, shared reference sites, and aligned uncertainty budgets. Finally, joint airborne campaigns would provide high-quality reference measurements under controlled conditions, enabling cross-mission performance assessment and supporting algorithm refinement. Collectively, these measures would establish a coherent framework for maximizing scientific return and ensuring sustained interoperability among the three missions.

7 Conclusion

The TRISHNA mission is designed to address a long-standing gap in thermal infrared Earth observation by combining high spatial resolution multispectral TIR measurements (60 m) with wide swath coverage and frequent revisit of 3 days, thereby supporting systematic monitoring of surface energy processes at scales relevant to natural and managed ecosystems. This concept has become possible thanks to recent advances in thermal infrared instrumentation and mission concepts, which have opened new perspectives for land surface temperature monitoring, enabling observations that were previously limited by constraints on spatial resolution, revisit frequency, and radiometric performance.

The mission concept was carefully elaborated through an integrated design approach—linking orbit configuration, spectral definition, viewing geometry, and calibration strategy—to meet the stringent requirements imposed by applications such as evapotranspiration estimation, vegetation water stress monitoring, and coastal and inland water observations. The simultaneous acquisition of VNIR, SWIR, and TIR data will enable physically consistent retrievals of key surface variables, while ensuring compatibility with past and future Earth observation missions. In particular, TRISHNA is positioned to operate in strong synergy with existing and forthcoming high-resolution thermal missions, including LSTM and EAGLE-TIR, contributing to improved temporal sampling, cross-calibration opportunities, and long-term continuity of land surface temperature records.

Overall, the TRISHNA mission exemplifies the transition toward a new generation of thermal infrared Earth observation systems, in which improved spatial detail, temporal revisit, and radiometric consistency jointly support both scientific advances and operational applications. The data products anticipated from this mission will provide a valuable foundation for future research and applications in land surface process monitoring, climate adaptation, and sustainable resource management.

https://doi.org/10.5194/egusphere-2026-4492
Preprint. Discussion started: 31 July 2026

8 Code and data availability

No mission data are publicly available at the time of publication because the satellite is currently under development. Following launch and commissioning phase, the mission products will be distributed through the Bhoonidhi and GEODES data portals. Information on data access will be provided on the mission website (cnes.fr/en/projects/trishna). The Algorithm Theoretical Basis Documents (ATBDs) describing the scientific data products will be published separately. In addition, the prototype processor for the generation of the TRISHNA evapotranspiration products is being prepared for open-source release.

9 Author contributions

PG prepared the manuscript with key structural contributions from TV. CS, JLRa and MS described the system and ground segment. DA and LB contributed to the description of the visible and thermal instruments, respectively. JS and TV focused on the design of the thermal bands. SMa and RB described Level 1 algorithms. Level 2 algorithms and atmospheric corrections were explained by SMa, MM, ED, VR, RG, MP and OH.

Specific scientific sections and products were supported by: BB, JD, OM and GB (evapotranspiration); JLRo (albedo, radiation, directionality); JM (directionality); JLT (albedo); AO, KM, ES, JE, NF, AD and SMw (ecosystem stress algorithms and products); MW and AS (vegetation variables); EA, HY, ID, SSP, TT, JFP and CV (coastal and inland waters); LR, AR and JS (urban applications); GP, SG, SA, AK, KN and SKS (cryosphere); and MI, JA, BC, BSS, MV and RN (calibration/validation). Finally, IB described the synergy between missions and orbits and PM the overall scientific strategy.

10 Competing interests

The authors declare that they have no known competing financial interests or personal relationships that could have appeared to influence the work reported in this paper.

11 Disclaimer

Copernicus Publications remains neutral with regard to jurisdictional claims made in the text, published maps, institutional affiliations, or any other geographical representation in this paper. While Copernicus Publications makes every effort to include appropriate place names, the final responsibility lies with the authors. Views expressed in the text are those of the authors and do not necessarily reflect the views of the publisher.

12 Aknowledgement

The authors wish to express their sincere gratitude and appreciation to Jean-Pierre Lagouarde, retired researcher from INRAE. The realization of the TRISHNA mission owes much to his outstanding scientific contributions in the physics of thermal infrared remote sensing and its applications to ecosystem stress, and to his unwavering commitment over several decades to advancing the mission within the scientific community, engaging decision-makers, and fostering the support of space agencies. His vision, dedication, and perseverance have played a pivotal role in bringing the mission to fruition.

https://doi.org/10.5194/egusphere-2026-4492
Preprint. Discussion started: 31 July 2026

13 References

Abrams, M., Hook, S., and Ramachandran, B.: ASTER user handbook, IEEE Transactions on Geoscience and Remote Sensing, 2002.

Agam, N., Kustas, W. P., Anderson, M. C., Li, F., and Colaizzi, P. D.: Utility of thermal sharpening over Texas High Plains irrigated agricultural fields, J. Geophys. Res. Atmos., 112, D19110, 2007.

Alfieri, J. G., Anderson, M. C., Kustas, W. P., and Cammalleri, C.: Effect of the revisit interval and temporal upscaling methods on the accuracy of remotely sensed evapotranspiration estimates, Hydrol. Earth Syst. Sci., 21, 83–98, https://doi.org/10.5194/hess-21-83-2017, 2017.

Allen, R. G., Tasumi, M., and Trezza, R.: Satellite-based energy balance for mapping evapotranspiration with internalized calibration (METRIC)—Model, J. Irrig. Drain. Eng., 133, 380–394, https://doi.org/10.1061/(ASCE)0733-9437(2007)133:4(380), 2007.

Allies, A., Demarty, J., Olioso, A., Bouzou Moussa, I., Issoufou, H. B.-A., Velluet, C., Bahir, M., Mainassara, I., Oï, M., Chazarin, J.-P., and Cappelaere, B.: Evapotranspiration estimation in the Sahel using a new ensemble-contextual method, Remote Sens., 12, 380, https://doi.org/10.3390/rs12030380, 2020.

Allies, A., Olioso, A., Cappelaere, B., Boulet, G., Etchanchu, J., Barral, H., Bouzou Moussa, I., Chazarin, J.-P., Delogu, E., Issoufou, H. B.-A., Mainassara, I., Oï, M., and Demarty, J.: A remote sensing data fusion method for continuous daily evapotranspiration mapping at kilometric scale in Sahelian areas, J. Hydrol., 607, 127504, https://doi.org/10.1016/j.jhydrol.2022.127504, 2022.

Alonso-González, M., et al.: OSSE analysis of TRISHNA LST assimilation impact on snow water equivalent modelling, technical report / manuscript, 2023.

Anderson, M. C., Allen, R. G., Morse, A., and Kustas, W. P.: Use of Landsat thermal imagery in monitoring evapotranspiration and managing water resources, Remote Sens. Environ., 122, 50–65, https://doi.org/10.1016/j.rse.2011.08.025, 2012.

Anderson, M. C., Norman, J. M., Kustas, W. P., Houborg, R., Starks, P. J., and Agam, N.: A thermal-based remote sensing technique for routine mapping of land-surface carbon, water and energy fluxes from field to regional scales, Remote Sensing of Environment, 112, 4227–4241, https://doi.org/10.1016/j.rse.2008.07.009, 2008.

Anderson, M. C., Norman, J. M., Mecikalski, J. R., Otkin, J. A., and Kustas, W. P.: A climatological study of evapotranspiration and moisture stress across the continental United States based on thermal remote sensing: Model formulation, J. Geophys. Res., 112, D10117, https://doi.org/10.1029/2006JD007506, 2007.

Arnfield, A. J.: Two decades of urban climate research: a review of turbulence, exchanges of energy and water, and the urban heat island, Int. J. Climatol., 23, 1–26, https://doi.org/10.1002/joc.859, 2003.

Bacour, C., Baret, F., Beal, D., Weiss, M., and Pavageau, K.: Neural network estimation of LAI, fAPAR, fCover and LAIxCab from top-of-canopy MERIS reflectance data: principles and validation, Remote Sens. Environ., 105, 313–325, 2006.

Baetens, L., Desjardins, C., and Hagolle, O.: Validation of Copernicus Sentinel-2 cloud masks obtained from MAJA, Sen2Cor, and Fmask processors, Remote Sens., 11, 433, 2019.

Barsi, J. A., Markham, B. L., Schott, J. R., Hook, S. J., and Raqueno, N. G.: Twenty-five years of landsat thermal band calibration, 2010 IEEE International Geoscience and Remote Sensing Symposium (IGARSS), Honolulu, HI, USA, 2287–2290, https://doi.org/10.1109/IGARSS.2010.5652528, 2010.

Baschek, B., and Molemaker, M. J.: Aerial and in situ measurements of submesoscale eddies, fronts and filaments, Ocean Sciences Meeting, Portland, USA, 2010.

https://doi.org/10.5194/egusphere-2026-4492
Preprint. Discussion started: 31 July 2026

Bastiaanssen, W. G. M., Menenti, M., Feddes, R. A., and Holtslag, A. A. M.: A remote sensing surface energy balance algorithm for land (SEBAL) – 2. Validation, Journal of Hydrology, 213, 198–212, https://doi.org/10.1016/S0022-1694(98)00253-4, 1998.

Bastiaanssen, W. G. M., Menenti, M., Feddes, R. A., and Holtslag, A. A. M.: A remote sensing surface energy balance algorithm for land (SEBAL): 1. Formulation, J. Hydrol., 212–213, 198–212, https://doi.org/10.1016/S0022-1694(98)00253-4, 1998.

Bayer, T. K., Burns, C. W., and Schallenberg, M.: Application of a numerical model to predict impacts of climate change on water temperatures in two deep, oligotrophic lakes in New Zealand, Hydrobiologia, 713, 53–71, 2013.

Bechtel, B., Zakšek, K., and Hoshyaripour, G.: Downscaling land surface temperature in an urban area: a case study for Hamburg, Germany, Remote Sens., 4, 3184–3200, https://doi.org/10.3390/rs4103184, 2012.

Behrenfeld, M., O'Malley, R., Siegel, D., McClain, C., Sarmiento, J., Feldman, G., Milligan, A., Falkowski, P., Letelier, R., and Boss, E.: Climate-driven trends in contemporary ocean productivity, Nature, 444, 752–755, https://doi.org/10.1038/nature05317, 2006.

Benn, D. I., and Evans, D. J. A.: Glaciers and Glaciation, Hodder Education, London, 2010.

Berni, J. A. J., Zarco-Tejada, P. J., Sepulcre-Cantó, G., Fereres, E., and Villalobos, F.: Mapping canopy conductance and CWSI in olive orchards using high resolution thermal remote sensing imagery, Remote Sens. Environ., 113, 2380–2388, https://doi.org/10.1016/j.rse.2009.06.018, 2009.

Bhambri, R., Bolch, T., Kawishwar, P., Dobhal, D. P., Srivastava, D., and Pratap, B.: Heterogeneity in glacier response in the upper Shyok valley, northeast Karakoram, The Cryosphere, 7, 1385–1398, 10.5194/tc-7-1385-2013, 2013.

Bhattacharya, B. K. and Chattopadhyay, C.: A multi-stage tracking for mustard rot disease combining surface meteorology and satellite remote sensing, Computers and Electronics in Agriculture, 90, 35–44, 2013.

Bhattacharya, B. K. and Nigam, R.: Development of Satellite-based Operational Agro-met Products for Value-added Agro-met Advisories, in: Agrometeorological Applications for Climate Resilient Agriculture, edited by: Chattopadhyay, N., Stefanski, R., Attri, S. D., and Rathore, L. S., Capital Publishing Company, co-published by Springer and International Publishing, Cham, Switzerland, 337–350, ISBN 978-93-818-91-15-5, 2024.

Bhattacharya, B. K., Mallick, K., Desai, D., Bhat, G. S., Morrison, R., Clevery, J. R., Woodgate, W., Beringer, J., Cawse-Nicholson, K., Ma, S., Verfaillie, J., and Baldocchi, D.: A coupled ground heat flux–surface energy balance model of evaporation using thermal remote sensing observations, Biogeosciences, 19, 5521–5551, 2022.

Bhattacharya, B. K., Mallick, K., Nigam, R., Dakore, K., and Shekh, A. M.: Efficiency based wheat yield prediction in a semi-arid climate using energy budgeting with satellite observations, Agricultural and Forest Meteorology, 151, 1394–1408, 2011.

Bojinski, S., Verstraete, M., Peterson, T. C., Richter, C., Simmons, A., and Zemp, M.: The Concept of Essential Climate Variables in Support of Climate Research, Applications, and Policy, Bulletin of the American Meteorological Society, 95, 1431–1443, https://doi.org/10.1175/BAMS-D-13-00047.1, 2014.

Boulet, G., Chehbouni, A., Gentine, P., Duchemin, B., Ezzahar, J., and Hadria, R.: Monitoring water stress using time series of observed to unstressed surface temperature difference, Agricultural and Forest Meteorology, 146, 159–172, https://doi.org/10.1016/j.agrformet.2007.05.012, 2007.

Boulet, G., Mougenot, B., Lhomme, J.-P., Fanise, P., Lili-Chabaane, Z., Olioso, A., Bahir, M., Rivalland, V., Jarlan, L., Merlin, O., Coudert, B., Er-Raki, S., and Lagouarde, J.-P.: The SPARSE model for the prediction of water stress and evapotranspiration components from thermal infra-red data and its evaluation over irrigated and rainfed wheat, Hydrology and Earth System Science, 19, 4653–4672, https://doi.org/10.5194/hess-19-4653-2015, 2015.

Brahmbhatt, R. M., Bahuguna, I. M., Rathore, B. P., Singh, S. K., Rajawat, A. S., Shah, R. D., and Kargel, J. S.: Satellite monitoring of glaciers in the Karakoram from 1977 to 2013: an overall almost stable population of dynamic glaciers, The Cryosphere Discussions, 9, 1–38, https://doi.org/10.5194/tcd-9-1555-2015, 2015.

Brando, V. E., Braga, F., Zaggia, L., Giardino, C., Bresciani, M., Matta, E., ... and Carniel, S.: High-resolution satellite turbidity and sea surface temperature observations of river plume interactions during a significant flood event, Ocean Science, 11, 909–920, 2015.

Cahyono, A. B., Saptarini, D., Pribadi, C. B., and Armono, H. D.: Estimation of Sea Surface Temperature(SST) Using Split Window Methods for Monitoring Industrial Activity in Coastal Area, Applied Mechanics and Materials, 862, 90, 2017.

Cao, B., Roujean, J.-L., Gastellu-Etchegorry, J.-P., Liu, Q., Du, Y., Lagouarde, J.-P., Huang, H., Li, H., Bian, Z., Hu, T., Qin, B., Ran, X., and Xiao, Q.: A general framework of kernel-driven modeling in the thermal infrared domain, Remote Sens. Environ., 252, 112157, 2021.

Capet, X., McWilliams, J. C., Molemaker, M. J., and Shchepetkin, A. F.: Mesoscale to submesoscale transition in the California current system: Part I: Flow structure, eddy flux, and observational tests, J. Phys. Oceanogr., 38, 29–43, https://doi.org/10.1175/2007JPO3671.1, 2008.

Carlson, T. N., and Arthur, S. T.: The impact of land use–land cover changes due to urbanization on surface microclimate and hydrology: a satellite perspective, Glob. Planet. Change, 25, 49–65, https://doi.org/10.1016/S0921-8181(00)00021-7, 2000.

Carlson, T. N.: An overview of the triangle method for estimating surface evapotranspiration and soil moisture from satellite imagery, Sensors, 7, 1612–1629, https://doi.org/10.3390/s7081612, 2007.

Carn, S. A., Krueger, A. J., Krotkov, N. A., and Yang, K.: Satellite-based constraints on volcanic sulfur dioxide emissions using ultraviolet and infrared sensors, J. Geophys. Res., 113, 2008.

Carrer, D., et al.: Daily estimates of aerosol optical thickness over land surface based on directional and temporal analysis of SEVIRI MSG visible observations, J. Geophys. Res. Atmos., 115, D10208, 2010.

Caselles, V., Rubio, E., Coll, C., and Valor, E.: Thermal band selection for the PRISM instrument: optimal band configurations, J. Geophys. Res. Atmos., 103, 17057–17067, 1998.

Cawse-Nicholson, K., Abrams, M., Buongiorno, M. F., Freeborn, D., Gamet, P., Gottfriedsen, J., and Fisher, J. B.: Current and future high-resolution multi-channel thermal imagers, in: High Spatio-Temporal-Spectral Thermal Remote Sensing, edited by: Peng Gong, CRC Press, 37–60, https://doi.org/10.1201/9781003458562-4, 2026.

Chakraborty, S. D., Kant, Y., and Mitra, D.: Assessment of land surface temperature and heat fluxes over Delhi using remote sensing data, J. Environ. Manage., 148, 143–152, https://doi.org/10.1016/j.jenvman.2013.11.034, 2015.

Charvet, D., et al.: TRISHNA TIR instrument development and performance status, International Conference on Space Optics - ICSO 2022, October 2022.

Chelton, D. B., M. G. Schlax, and R. M. Samelson: Summertime Coupling between Sea Surface Temperature and Wind Stress in the California Current System, J. Phys. Oceanogr., 37, 495–517, https://doi.org/10.1175/JPO3025.1, 2007.

Chelton, D. B., Schlax, M. G., and Samelson, R. M.: Summertime coupling between sea surface temperature and wind stress in the California Current System, J. Phys. Oceanogr., 37, 495–517, https://doi.org/10.1175/JPO3025.1, 2007.

Cheng, K. H., Luo, X., and Jiao, J. J.: Two-decade variations of fresh submarine groundwater discharge to Tolo Harbour and their ecological significance by coupled remote sensing and radon-222 model, Water Research, 178, 115866, 2020.

Chevallier, F., Chedin, A., Cheruy, F., and Morcrette, J. J.: TIGR-like atmospheric-profile databases for accurate radiative-flux computation, Q. J. R. Meteorol. Soc., 126, 777–785, 2000.

Choudhury, I. and Bhattacharya, B.: Decadal gross level assessment of green and blue consumptive water use over Indian agro-ecosystems, International Journal of Remote Sensing, 42, 6628–6669, 2021.

Corbari, C. and Mancini, M.: Irrigation efficiency optimization at multiple stakeholders' levels based on remote sensing data and energy water balance modelling, Irrigation Science, 41, 121–139, 2023.

Courault, D., Seguin, B., and Olioso, A.: Review on estimation of evapotranspiration from remote sensing data: From empirical to numerical modeling approaches, Irrigation and Drainage Systems, 19, 223–249, https://doi.org/10.1007/s10795-005-5186-0, 2005.

Crebassol, P., Lagouarde, J. P., and Hook, S. J.: Thirsty thermal infrared spatial system, 2014 IEEE Geoscience and Remote Sensing Symposium (IGARSS), Quebec City, QC, Canada, 3021–3024, https://doi.org/10.1109/IGARSS.2014.6947113, 2014.

Crow, W. T., Kustas, W. P., and Prueger, J. H.: Monitoring root-zone soil moisture through the assimilation of a thermal remote sensing-based soil moisture proxy into a water balance model, Remote Sens. Environ., 112, 1268–1281, https://doi.org/10.1016/j.rse.2006.11.033, 2008.

Crow, W. T., Ryu, D., and Entekhabi, D.: Evaluating the assimilation of remotely sensed soil moisture retrievals into a land surface model using the ensemble Kalman filter, J. Hydrometeorol., 9, 461–474, 2008.

Danis, P. A., Von Grafenstein, U., Masson-Delmotte, V., Planton, S., Gerdeaux, D., and Moisselin, J. M.: Vulnerability of two European lakes in response to future climatic changes, Geophysical Research Letters, 31, 2004.

Daufresne, M., Lengfellner, K., and Sommer, U.: Global warming benefits the small in aquatic ecosystems, Proceedings of the National Academy of Sciences, 106, 12788–12793, 2009.

De Ridder, K., and Lefebre, P.: Urban heat island and urban climate studies: methodology and case study in the Ruhr area, VITO Report (BUGS project), 2004.

Dean, K. G., Stringer, W. J., Ahlnäs, K., Searcy, C., and Weingartner, T.: The influence of sea ice on the marine climate of the Bering Sea, J. Geophys. Res., 99, 22441–22457, https://doi.org/10.1029/94JC01763, 1994.

Dehn, J., Dean, K. J., Engle, K., and Izbekov, P.: Thermal precursors in satellite images of the 1999 eruption of Shishaldin Volcano, Bull. Volcanol., 64, 525–534, https://doi.org/10.1007/s00445-002-0227-0, 2002.

Delogu, E., Olioso, A., Allies, A., Demarty, J., and Boulet, G.: Evaluation of multiple methods for the production of continuous evapotranspiration estimates from TIR remote sensing, Remote Sens., 13, 1086, https://doi.org/10.3390/rs13061086, 2021.

Delogu, E., Olioso, A., Jacob, F., et al.: Temporal variations of evapotranspiration: reconstruction using instantaneous satellite measurements in the thermal infrared domain, Hydrology and Earth System Sciences, 16, 1699–1740, https://doi.org/10.5194/hess-16-1699-2012, 2012.

Dominguez, A., Kleissl, J., Luvall, J. C., and Rickman, D. L.: High-resolution urban thermal sharpener (HUTS), Remote Sens. Environ., 115, 1772–1780, https://doi.org/10.1016/j.rse.2011.03.008, 2011.

Donlon, C. J., et al.: Successes and challenges for the modern Sea Surface Temperature Observing System: The GHRSST Development and Implementation Plan (GDIP), OceanObs'09 Conference, Venice, 45 pp., 2009.

Dousset, B., Gourmelon, F., Laaidi, K., Zeghnoun, A., Giraudet, E., Bretin, P., Mauri, E., and Vandentorren, S.: Satellite monitoring of summer heat waves in the Paris metropolitan area, Int. J. Climatol., 31, 313–323, https://doi.org/10.1002/joc.2222, 2011.

Drusch, M., et al.: Sentinel-2: ESA's optical high-resolution mission for GMES operational services, Remote Sens. Environ., 120, 25–36, 2012.

Duffour, C., Lagouarde, J.-P., and Roujean, J.-L.: A two-parameter model to simulate thermal infrared directional effects, Remote Sens. Environ., 186, 250–261, 2016.

https://doi.org/10.5194/egusphere-2026-4492
Preprint. Discussion started: 31 July 2026

Duveiller, G., Weiss, M., Baret, F., and Defourny, P.: Retrieving wheat Green Area Index during the growing season from optical time series measurements based on neural network radiative transfer inversion, Remote Sens. Environ., 115, 887–896, 2011.

Eswar, R., Sekhar, M., and Bhattacharya, B. K.: A simple model for spatial disaggregation of evaporative fraction: Comparative study with thermal sharpened land surface temperature data over India, Journal of Geophysical Research Atmospheres, 118, 12029–12044, 2013.

European Commission: Commission Delegated Regulation (EU) No 1159/2013 on Copernicus data policy, Official Journal of the European Union, 2013.

FAO: Crop yield response to water, FAO Irrigation and Drainage Paper 66, Food and Agriculture Organization of the United Nations, Rome, https://www.fao.org/3/i2800e/i2800e.pdf, 2009.

Farhani, N.: Apport de la télédétection et des variables auxiliaires dans l'étude de l'évolution des périodes de sécheresse, PhD thesis, Université Paul Sabatier – Toulouse III / Université de Carthage, https://theses.hal.science/tel-03715302v1, 2022.

Farinotti, D., Longuevergne, L., Moholdt, G., Duethmann, D., Mölg, T., Bolch, T., Vorogushyn, S., and Güntner, A.: Substantial glacier mass loss in the Tien Shan over the past 50 years, Nature Geoscience, 8, 716–722, 10.1038/NGEO2513, 2015.

Fisher, J. B., Lee, B., Purdy, A. J., Halverson, G. H., and Dohlen, M. B.: ECOSTRESS: NASA's next generation mission to measure evapotranspiration from the International Space Station, Water Resources Research, 56, e2019WR026058, https://doi.org/10.1029/2019WR026058, 2020.

Fu, L.-L., and Ferrari, R.: Observing oceanic submesoscale processes from space, Eos Trans. AGU, 89, 488, https://doi.org/10.1029/2008EO480003, 2008.

Gallego-Elvira, B., Olioso, A., Mira, M., Reyes Castillo, S., Boulet, G., Marloie, O., Garrigues, S., Courault, D., Weiss, M., Chauvelon, P., and Boutron, O.: EVASPA (EVapotranspiration Assessment from SPAce) tool: an overview, Procedia Environ. Sci., 19, 303–310, https://doi.org/10.1016/j.proenv.2013.06.035, 2013.

Galleguillos, M., Jacob, F., Prévot, L., French, A., and Lagacherie, P.: Comparison of two temperature differencing methods to estimate daily evapotranspiration over a Mediterranean vineyard watershed from ASTER data, Remote Sens. Environ., 115, 1326–1340, https://doi.org/10.1016/j.rse.2011.01.013, 2011.

Gao, B.-C. and Kaufman, Y. J.: Selection of the 1.375-µm MODIS channel for cirrus cloud detection, J. Atmos. Ocean. Technol., 12, 918–925, 1995.

García, L., Parra, L., Jimenez, JM., Lloret, J., and Lorenz, P.: IoT-Based Smart Irrigation Systems: An Overview on the Recent Trends on Sensors and IoT Systems for Irrigation in Precision Agriculture, Sensors, 20, 1042, https://doi.org/10.3390/s20041042, 2020.

Gardelle, J., Berthier, E., Arnaud, Y., and Kääb, A.: Region-wide glacier mass balances over the Pamir–Karakoram–Himalaya during 1999–2011, The Cryosphere, 7, 1263–1286, https://doi.org/10.5194/tc-7-1263-2013, 2013.

Garrigues, S., Allard, D., Baret, F., and Weiss, M.: Remote sensing of vegetation variables, Remote Sens. Environ., 103, 81–96, 2006.

GCOS: The Global Climate Observing System 2021: The GCOS Status Report (GCOS-240), WMO, Geneva, 2021.

Geiger, B., et al.: Surface albedo derived from Meteosat Second Generation SEVIRI using LSA-SAF algorithms, LSA-SAF technical documentation, 2008.

Gentine, P., Entekhabi, D., Chehbouni, A., Boulet, G., and Duchemin, B.: Analysis of evaporative fraction diurnal behavior, Agric. For. Meteorol., 143, 13–29, https://doi.org/10.1016/j.agrformet.2006.11.002, 2007.

Gerhards, M., Schlerf, M., Mallick, K., and Udelhoven, T.: Challenges and Future Perspectives of Multi-/Hyperspectral Thermal Infrared Remote Sensing for Crop Water-Stress Detection: A Review, Remote Sens., 11, 1240, https://doi.org/10.3390/rs11101240, 2019.

Gerland, S., Winther, J. G., Ørbæk, J. B., Liston, G. E., Oritsland, N. A., Blanco, A., and Ivanov, B.: Physical and optical properties of snow covering Arctic tundra on Svalbard, Hydrological Processes, 13, 2331–2343, 1999.

Gillespie, A., Rokugawa, S., Matsunaga, T., Cothern, J. S., Hook, S., and Kahle, A. B.: A temperature and emissivity separation algorithm for ASTER images, IEEE Trans. Geosci. Remote Sens., 36, 1113–1126, https://doi.org/10.1109/36.700995, 1998.

Govaerts, Y. M., et al.: Method for the retrieval of surface albedo from SEVIRI observations, J. Geophys. Res. Atmos., 113, D16108, https://doi.org/10.1029/2007JD009191, 2008.

Grierson, I. T.: Use of airborne thermal imagery to detect and monitor inshore oil spill residues during darkness hours, Environ. Manage., 22, 905–912, https://doi.org/10.1007/s002679900157, 1998.

Grimmond, C. S. B., et al.: Initial results from Phase 2 of the international urban energy balance model comparison, Int. J. Climatol., 31, 244–272, https://doi.org/10.1002/joc.2227, 2011.

Gruson, L., Jacob, F., Olioso, A., Gamet, P., and Labarre, L.: Instrumental performance requirements for the design of the micro-bolometer-based TRISHNA thermal infrared sensor: simulation-based error budget of the TES method, presented at SPIE Sensors, Systems, and Next-Generation Satellites XXIV, online, 21–25 September 2020.

Guha, A., and Vinod Kumar, K.: New ASTER derived thermal indices to delineate mineralogy of different granitoids of an Archaean craton, Ore Geol. Rev., 74, 76–87, https://doi.org/10.1016/j.oregeorev.2015.10.033, 2016.

Guillevic, P. C., Olioso, A., Hook, S. J., Fisher, J. B., Lagouarde, J.-P., and Vermote, E. F.: Impact of the revisit of thermal infrared remote sensing observation on evapotranspiration uncertainty – A sensitivity study using AmeriFlux data, Remote Sensing, 11, 573, https://doi.org/10.3390/rs11050573, 2019.

Gutknecht, E., Dadou, I., Le Vu, B., Cambon, G., Sudre, J., Garçon, V., Machu, E., Rixen, T., Kock, A., Flohr, A., Paulmier, A., and Lavik, G.: Coupled physical/biogeochemical modeling including O_2-dependent processes in Eastern Boundary Upwelling Systems: application in the Benguela, Biogeosciences, 10, 3559–3591, https://doi.org/10.5194/bg-10-3559-2013, 2013.

Haggerty, J. A., Maslanik, J. A., and Curry, J. A.: Heterogeneity of sea ice surface temperature at SHEBA from aircraft measurements, J. Geophys. Res., 108, C10, 8052, https://doi.org/10.1029/2000JC000560, 2003.

Hagolle, O., Huc, M., Desjardins, C., and Auer, S.: MAJA Algorithm Theoretical Basis, 2017.

Hagolle, O., Huc, M., Villa Pascual, D., and Dedieu, G.: A multi-temporal method for cloud detection applied to FORMOSAT-2, VENμS, LANDSAT and SENTINEL-2 images, Remote Sens. Environ., 114, 1747–1755, 2010.

Hall, D. K., Key, J. R., Casey, A., Riggs, G. A., and Cavalieri, D. J.: Sea ice surface temperature product from MODIS, IEEE Transactions on Geoscience and Remote Sensing, 42, 1076–1087, 10.1109/TGRS.2004.825587, 2004.

Hall, D. K., Riggs, G. A., and Salomonson, V. V.: Development of methods for mapping global snow cover using MODIS data, Remote Sensing of Environment, 54, 127–140, 1995.

Han, X., Zhou, Q., Zhang, B., Che, Z., Qiu, R., Chen, H., Li, Y., and Du, T.: Real-time methods for short and medium-term evapotranspiration forecasting using dynamic crop coefficient and historical threshold, Journal of Hydrology, 606, 127414, https://doi.org/10.1016/j.jhydrol.2021.127414, 2022.

Han, Y. and Zhang, A.: Cryogenic technology for infrared detection in space, Scientific Reports, 12, 2345, https://doi.org/10.1038/s41598-022-06216-5, 2022.

Harris, A. J. L., Blake, S., Rothery, D. A., and Stevens, N. F.: A chronology of the 1991–1993 Mount Etna eruption using AVHRR data, Geophys. Res. Lett., 102, 7985–8003, https://doi.org/10.1029/96JB03388, 1997.

https://doi.org/10.5194/egusphere-2026-4492
Preprint. Discussion started: 31 July 2026

Hollstein, A., Segl, K., Guanter, L., and Brell, M.: Cloud detection using spectral and temporal features for Sentinel-2, Remote Sens. Environ. / ISPRS-related publication, 2015.

Holt, B., Baschek, B., Molemaker, J., Ohlmann, C., Smith, G., Marmorino, G., and Gierach, M.: Results from the Submesoscale Experiment-1 April 2011: in situ, aircraft and satellite measurements of small eddies, fronts, and filaments in the Southern California Bight, SEASAR 2012, Tromsø, Norway, 2012.

Hu, T., Mallick, K., Hitzelberger, P., Didry, Y., Boulet, G., Szantoi, Z., Koetz, B., Alonso, I., Pascolini-Campbell, M., Halverson, G., Cawse-Nicholson, K., Hulley, G. C., Hook, S., Bhattarai, N., Olioso, A., Roujean, J.-L., Gamet, P., and Su, B.: Evaluating European ECOSTRESS Hub evapotranspiration products across a range of soil-atmospheric aridity and biomes over Europe, Water Resour. Res., 59, e2022WR034132, https://doi.org/10.1029/2022WR034132, 2023.

Huret, M., Dadou, I., Dumas, F., Lazure, P., and Garçon, V.: Coupling physical and biogeochemical processes in the Rio de la Plata plume, Cont. Shelf Res., 25, 629–653, https://doi.org/10.1016/j.csr.2004.10.003, 2005.

IPCC: Climate Change 2013: The Physical Science Basis, Working Group I Contribution to the Fifth Assessment Report, Cambridge University Press, 2013.

IPCC: Climate Change 2014: Impacts, Adaptation, and Vulnerability, Cambridge University Press, Cambridge, https://www.ipcc.ch/report/ar5/wg2/, 2014.

Jacob, F., Vidal, T. H., Lesaignoux, A., Olioso, A., Weiss, M., Nerry, F., Jacquemoud, S., Gamet, P., Caillault, K., Labarre, L., et al.: A simulation-based error budget of the TES method for the design of the spectral configuration of the micro-bolometer-based MISTIGRI thermal infrared sensor, IEEE Trans. Geosci. Remote Sens., 2021.

Jiang, L., and Islam, S.: A methodology for estimation of surface evapotranspiration over large areas using remote sensing observations, Geophys. Res. Lett., 26, 2773–2776, https://doi.org/10.1029/1999GL006049, 1999.

Jung, M., Koirala, S., Weber, U., Ichii, K., Gans, F., Camps-Valls, G., Papale, D., Schwalm, C., Tramontana, G., and Reichstein, M.: The FLUXCOM ensemble of global land-atmosphere energy fluxes, Science Data, 6, 74, 2019.

Kalma, J. D., McVicar, T. R., and McCabe, M. F.: Estimating land surface evapotranspiration: A review of methods using remotely sensed surface temperature data, Surveys in Geophysics, 29, 421–469, https://doi.org/10.1007/s10712-008-9037-z, 2008.

Kherollah Pour, H., Duguay, C. R., Martynov, A., and Brown, L. C.: Simulation of surface temperature and ice cover of large northern lakes with 1-D models: comparison with MODIS data and in situ measurements, Tellus A, 64, 17614, https://doi.org/10.3402/tellusa.v64i0.17614, 2012.

Koetz, B., Bastiaanssen, W., Berger, M., Defourney, P., Del Bello, U., Drusch, M., Drinkwater, M., Duca, R., Fernandez, V., Ghent, D., Guzinski, R., Hoogeveen, J., Hook, S., Lagouarde, J.-P., Lemoine, G., Manolis, I., Martimort, P., Masek, J., Massart, M., Notarnicola, C., Sobrino, J., and Udelhoven, T.: High Spatio-Temporal Resolution Land Surface Temperature Mission - a Copernicus Candidate Mission in Support of Agricultural Monitoring, IGARSS 2018 - 2018 IEEE International Geoscience and Remote Sensing Symposium, Valencia, Spain, 8160–8162, https://doi.org/10.1109/IGARSS.2018.8517433, 2018.

Kulkarni, A. V., Singh, S. K., Mathur, P., and Mishra, V. D.: Algorithm to monitor snow cover using AWiFS data of RESOURCESAT-1 for the Himalayan region, International Journal of Remote Sensing, 27, 2449–2457, https/doi.org/10.1080/01431160500497820, 2006.

Kuroda, H. and Toya, Y.: High-Resolution Sea Surface Temperatures Derived from Landsat 8: A Study of Submesoscale Frontal Structures on the Pacific Shelf off the Hokkaido Coast, Japan, Remote Sensing, 12, 3326, 2020.

Kustas, W. P., and Norman, J. M.: Evaluation of soil and vegetation heat flux predictions using a simple two-source model with radiometric temperatures for partial canopy cover, Agric. For. Meteorol., 94, 13–29, https://doi.org/10.1016/S0168-1923(99)00005-2, 1999.

https://doi.org/10.5194/egusphere-2026-4492
Preprint. Discussion started: 31 July 2026

Kustas, W. P., Li, F., Jackson, T. J., Prueger, J. H., MacPherson, J. I., and Wolde, M.: Effects of remote sensing pixel resolution on modeled energy flux variability of croplands in Iowa, Remote Sens. Environ., 92, 535–547, 2004.

Lagouarde, J. P., Bach, M., Sobrino, J. A., Boulet, G., Briottet, X., Cherchali, S., and Fargant, G.: The MISTIGRI thermal infrared project: scientific objectives and mission specifications, International Journal of Remote Sensing, 34, 3437–3466, https://doi.org/10.1080/01431161.2012.716921, 2013.

Lagouarde, J.-P. and Irvine, M.: Directional anisotropy in thermal infrared measurements over Toulouse city centre, Meteorol. Atmos. Phys., 102, 173–185, 2008.

Lagouarde, J.-P., Hénon, A., Kurz, B., Moreau, P., Irvine, M., Voogt, J., and Mestayer, P.: Modelling daytime thermal infrared directional anisotropy over Toulouse city centre, Remote Sens. Environ., 114, 87–105, https://doi.org/10.1016/j.rse.2009.08.012, 2010a.

Lagouarde, J.-P., Olioso, A., Roujean, J.-L., Boulet, G., Coudert, B., Dayau, S., Castillo, S., and Weiss, M.: Defining the revisit frequency for the MISTIGRI project of a satellite mission in the thermal infrared, Proc. 3rd Int. Symp. Recent Advances in Quantitative Remote Sensing, Valencia, Spain, 824–829, 2010b.

Lagouarde, J.-P., Hénon, A., Irvine, M., Voogt, J., Pigeon, G., Moreau, P., Masson, V., and Mestayer, P.: Experimental characterization and modelling of the nighttime directional anisotropy of thermal infrared measurements over an urban area, Remote Sens. Environ., 117, 19–33, https://doi.org/10.1016/j.rse.2011.06.022, 2012.

Lagouarde, J.-P., Bach, M., Sobrino, J. A., Boulet, G., Briottet, X., Cherchali, S., Coudert, B., Dadou, I., Dedieu, G., Gamet, P., et al.: The MISTIGRI thermal infrared project: scientific objectives and mission specifications, Int. J. Remote Sens., 34, 3437–3466, 2013.

Lagouarde, J.-P., Irvine, M., and Dupont, S.: Impact of atmospheric turbulence on the accuracy of land surface temperature (LST) measurements, 3rd GlobTemperature User Consultation Meeting, European Space Agency (ESA), Reading, United Kingdom, June 2015, hal-02795610, 2015.

Lagouarde, J.P. and Boulet, G., 10. Energy Balance of Continental Surfaces and the Use of Surface Temperature by Jean-Pierre Lagouarde and Gilles Boulet, book Land Surface Remote Sensing in Continental Hydrology in Remote Sensing Observations of Continental Surfaces Book Set Edited by Nicolas Baghdadi, IRSTEA, France Mehrez Zribi, CNRS, France; ISBN: 9781785481048; Publication Date: September 2016 Hardback 502 pp. ; ISTE_ELSEVIER ; http://iste.co.uk/index.php?f=a&ACTION=View&id=1031.

Lagouarde, J.-P., Bhattacharya, B. K., Crébassol, P., Gamet, P., Adlakha, D., Murthy, C. S., Singh, S. K., Mishra, M., Nigam, R., Raju, P. V., Babu, S. S., Shukla, M. V., Pandya, M. R., Boulet, G., Briottet, X., Dadou, I., Dedieu, G., Gouhier, M., Hagolle, O., Irvine, M., Jacob, F., Kumar, K. K., Laignel, B., Maisongrande, P., Mallick, K., Olioso, A., Ottlé, C., Roujean, J.-L., Sobrino, J., Ramakrishnan, R., Sekhar, M., and Sarkar, S. S.: Indo-French high-resolution thermal infrared space mission for Earth natural resources assessment and monitoring – concept and definition of TRISHNA, International Archives of the Photogrammetry, Remote Sensing and Spatial Information Sciences, XLII-3/W6, 403–407, https://doi.org/10.5194/isprs-archives-XLII-3-W6-403-2019, 2019.

Lakhiar, I. A., Yan, H., Zhang, C., Zhang, J., Wang, G., Deng, S., Syed, T. N., Wang, B., and Zhou, R.: A review of evapotranspiration estimation methods for climate-smart agriculture tools under a changing climate: vulnerabilities, consequences, and implications, Journal of Water and Climate Change, 16, 249–288, https://doi.org/10.2166/wcc.2024.048, 2025.

Lebègue, L., Greslou, D., Blanchet, G., de Lussy, F., Fourest, S., Martin, V., Latry, C., Kubik, P., Delvit, J.-M., Dechoz, C., and Amberg, V.: Pléiades-HR satellites image quality commissioning, Revue Française de Photogrammétrie et de Télédétection, 210, 43–51, https://doi.org/10.52638/rfpt.2015.137, 2015.

Lee, C. M., Cable, M. L., Hook, S. J., Green, R. O., Ustin, S. L., Mandl, D. J., and Middleton, E. M.: An introduction to the NASA Hyperspectral InfraRed Imager (HyspIRI) mission and preparatory activities, Remote Sensing of Environment, 167, 6–19, https://doi.org/10.1016/j.rse.2015.06.012, 2015.

León-Tavares, J., Gómez-Dans, J., Roujean, J.-L., and Bruniquel, V.: Retrieving land surface reflectance anisotropy with Sentinel-3 observations and prior BRDF model constraints, Remote Sens. Environ., 302, 113967, https://doi.org/10.1016/j.rse.2023.113967, 2024.

Li, R.-R., Kaufman, Y. J., Gao, B.-C., and Davis, C. O.: Remote sensing of suspended sediments and shallow coastal waters, IEEE Trans. Geosci. Remote Sens., 41, 559–566, https://doi.org/10.1109/TGRS.2003.810227, 2003.

Li, Z.-L., Tang, B.-H., Wu, H., Ren, H., Yan, G., Wan, Z., Trigo, I. F., and Sobrino, J. A.: Satellite-derived land surface temperature: current status and perspectives, Remote Sensing of Environment, 131, 14–37, https://doi.org/10.1016/j.rse.2012.12.008, 2013.

Liang, S.: Broadband albedo based on satellite data: a review and analysis of methods, Remote Sens. Rev., 20, 163–190, https://doi.org/10.1080/02757250310001136034, 2003.

Louchart, X., and Voltz, M.: Aging effects on herbicide availability for runoff transfer, Environmental Science & Technology, 41, 1137–1141, https://doi.org/10.1021/es061186q, 2007.

Maimaitiyiming, M., Ghulam, A., Tiyip, T., Pla, F., Carmona, P., Halik, Ü., and Caetano, M.: Effects of green space spatial pattern on land surface temperature: implications for sustainable urban planning, ISPRS J. Photogramm. Remote Sens., 89, 59–66, https://doi.org/10.1016/j.isprsjprs.2013.12.010, 2014.

Majumdar, T. J.: Geomorphological characteristics identification using thermal remote sensing and SAR interferometry, Nat. Hazards, 69, 729–747, https://doi.org/10.1007/s11069-013-0731-x, 2013.

Mallast, U., Schwonke, F., Gloaguen, R., Geyer, S., Sauter, M., and Siebert, C.: Airborne thermal data identifies groundwater discharge at the north-western coast of the Dead Sea, Remote Sens., 5, 6361–6381, https://doi.org/10.3390/rs5126361, 2013.

Mallick, K., Baldocchi, D., Jarvis, A., Hu, T., Trebs, I., Sulis, M., et al.: Insights into the aerodynamic versus radiometric surface temperature debate in thermal-based evaporation modeling, Geophys. Res. Lett., 49, e2021GL097568, https://doi.org/10.1029/2021GL097568, 2022.

Mallick, K., Bhattacharya, B. K., and Patel, N. K.: Estimating evapotranspiration using a trapezoidal model, Remote Sens. Environ., 150, 161–173, https://doi.org/10.1016/j.rse.2014.04.012, 2014.

Mallick, K., Bhattacharya, B. K., Rao, V. U. M., Reddy, D. R., Banerjee, S., Venkatesh, H., Pandey, V., Kar, G., Mukherjee, J., Vyas, S. P., Gadgil, A. S., and Patel, N. K.: Latent heat flux estimation in clear sky days over Indian agroecosystems using noontime satellite remote sensing data, Agric. For. Meteorol., 149, 1646–1665, https://doi.org/10.1016/j.agrformet.2009.05.006, 2009.

Mallick, K., Boegh, E., Trebs, I., Alfieri, J. G., Kustas, W. P., Prueger, J. H., Niyogi, D., Das, N., Drewry, D. T., Hoffmann, L., and Jarvis, A. J.: Reintroducing radiometric surface temperature into the Penman-Monteith formulation, Water Resour. Res., 51, 6214–6243, https://doi.org/10.1002/2014WR016106, 2015.

Mallick, K., Jarvis, A. J., Boegh, E., Fisher, J. B., Drewry, D. T., Tu, K. P., Hook, S. J., Hulley, G., Ardö, J., Beringer, J., Arain, A., and Niyogi, D.: A surface temperature initiated closure (STIC) for surface energy balance fluxes, Remote Sens. Environ., 141, 243–261, https://doi.org/10.1016/j.rse.2013.10.022, 2014.

Mallick, K., Toivonen, E., Trebs, I., Boegh, E., Cleverly, J., Eamus, D., Koivusalo, H., Drewry, D., Arndt, S. K., Griebel, A., and Beringer, J.: Bridging thermal infrared sensing and physically-based evapotranspiration modeling: from theoretical implementation to validation across an aridity gradient in Australian ecosystems, Water Resour. Res., 54, 3409–3435, https://doi.org/10.1029/2017WR021357, 2018.

Marcq, S., Delogu, E., Chapelier, M., and Vidal, T. H.: DirecTES: A direct method for land and sea surface temperature and emissivity separation for thermal infrared sensors—application to TRISHNA and ECOSTRESS, Remote Sens., 15, 517, 2023.

Markham, B. L., et al.: Landsat 8 operational land imager and thermal infrared sensor, Remote Sens. Environ., 185, 519–532, 2014.

Markham, B. L., Knight, E. J., Canova, B., Donley, E., and Kvaran, G.: The Landsat Data Continuity Mission Operational Land Imager (OLI) sensor, 2012 IEEE International Geoscience and Remote Sensing Symposium (IGARSS), Munich, Germany, 6995–6998, https://doi.org/10.1109/IGARSS.2012.6351961, 2012.

Martilli, A., Clappier, A., and Rotach, M. W.: An urban surface exchange parameterisation for mesoscale models, Bound.-Layer Meteorol., 104, 261–304, https://doi.org/10.1023/A:1016099921195, 2002.

Martinec, J.: Snowmelt runoff model for streamflow forecast, Nordic Hydrology, 6, 197–219, 1975.

Masson, V., Lemonsu, A., Hidalgo, J., and Voogt, J.: Urban Climates and Climate Change, Annu. Rev. Environ. Resour., 45, 411–444, https://doi.org/10.1146/annurev-environ-012320-083623, 2020.

Masson, V., Marchadier, C., Adolphe, L., Aguejdad, R., Avner, P., Bonhomme, M., Bretagne, G., Briottet, X., Bueno, B., De Munck, C., Doukari, O., Hallegatte, S., Hidalgo, J., Houet, T., Lemonsu, A., Long, N., Moine, M.-P., Morel, T., Nolorgues, L., Pigeon, G., Salagnac, J.-L., Viguié, V., and Zibouche, K.: Adapting cities to climate change: a systemic modelling approach, Urban Climate, https://doi.org/10.1016/j.uclim.2014.03.004, 2014.

Masson, V.: Urban surface modelling and the meso-scale impact of cities, Theor. Appl. Climatol., 84, 35–45, 2006.

Matricardi, M., Chevallier, F., Kelly, G., and Thépaut, J.-N.: An improved general fast radiative transfer model for the assimilation of radiance observations, ECMWF Technical Memorandum, 2001.

Matthews, M. W.: A current review of empirical procedures of remote sensing in inland and near-coastal transitional waters, Int. J. Remote Sens., 32, 6855–6899, https://doi.org/10.1080/01431161.2010.512947, 2011.

Mejías, M., Ballesteros, B. J., Antón-Pacheco, C., Domínguez, J. A., Garcia-Orellana, J., Garcia-Solsona, E., and Masqué, P.: Methodological study of submarine groundwater discharge from a karstic aquifer in the Western Mediterranean Sea, J. Hydrol., 464–465, 27–40, https://doi.org/10.1016/j.jhydrol.2012.06.020, 2012.

Michel, A., Granero-Belinchon, C., Cassante, C., Boitard, P., Briottet, X., Adeline, K. R. M., Poutier, L., and Sobrino, J. A.: A New Material-Oriented TES for Land Surface Temperature and SUHI Retrieval in Urban Areas: Case Study over Madrid in the Framework of the Future TRISHNA Mission, Remote Sens., 13, 5139, https://doi.org/10.3390/rs13245139, 2021.

Michel, J., Hagolle, O., Hook, S. J., Roujean, J.-L., and Gamet, P.: Quantifying thermal infrared directional anisotropy using MASTER and Landsat-8 simultaneous acquisitions, Remote Sens. Environ., 297, 113765, https://doi.org/10.1016/j.rse.2023.113765, 2023.

Mishra, M. K., Misra, A., and Kumar, R.: Operational AOD Retrieval at Subkilometer Resolution Using OceanSat-2 OCM Over Land: SAER Algorithm, Uncertainties, Validation & Inter-Sensor Comparison, Earth and Space Science, 10, e2023EA002896, 2023.

Moran, M. S., Clarke, T. R., Inoue, Y., and Vidal, A.: Estimating crop water deficit using the relation between surface-air temperature and spectral vegetation index, Remote Sens. Environ., 49, 246–263, https://doi.org/10.1016/0034-4257(94)90020-5, 1994.

Morfitt, R., Barsi, J., Levy, R., Markham, B., Micijevic, E., Ong, L., Scaramuzza, P., and Vanderwerff, K.: Landsat-8 Operational Land Imager (OLI) Radiometric Performance On-Orbit, Remote Sens., 7, 2208–2237, https://doi.org/10.3390/rs70202208, 2015.

https://doi.org/10.5194/egusphere-2026-4492
Preprint. Discussion started: 31 July 2026

Mu, Q., Zhao, M., and Running, S. W.: MODIS global terrestrial evapotranspiration (ET) product (MOD16) improvements and applications, Remote Sens., 5, 3365–3381, https://doi.org/10.3390/rs5073365, 2013.

Mukherjee, S., Joshi, P. K., and Garg, R. D.: Analysis of urban built-up areas and surface urban heat island using downscaled MODIS land surface temperature data, Geocarto Int., https://doi.org/10.1080/10106049.2016.1222634, 2016.

Mwangi, S., Boulet, G., and Olioso, A.: Assessment of an extended SPARSE model for estimating evapotranspiration from directional thermal infrared data, Agricultural and Forest Meteorology, 317, 108882, 10.1016/j.agrformet.2022.108882, 2022.

Navalgund, R. R., Jayaraman, V., and Roy, P. S.: Remote sensing applications: An overview, Current Science, 93, 1747–1766, 2007.

Nigam, R., Bhattacharya, B. K., and Pandya, M. R.: Satellite agromet products and their adaptation for advisory services to Indian farming community, Journal of Agrometeorology, 25, 42–50, 2023.

Nigam, R., Bhattacharya, B. K., Das, A., Kumar, M., and Kumar, P.: A geo-spatial assessment of desert locust risk over India during summer 2020 using GEO-LEO satellite observations and weather forecast, Remote Sensing Applications: Society and Environment, 41, 10183, 2026.

Ogawa, K., Schmugge, T. J., and Hook, S. J.: Estimation of surface thermal inertia from day–night satellite observations, Remote Sens. Environ., 90, 399–412, 2004.

Olioso, A., Allies, A., Boulet, G., Delogu, E., Demarty, J., Gallego-Elvira, B., Mira, M., Marloie, O., Chauvelon, P., Boutron, O., Buis, S., Weiss, M., Velluet, C., and Bahir, M.: Monitoring evapotranspiration from remote sensing data and ground data using ensemble model averaging, IGARSS, Valencia, 2018.

Olioso, A., Bahir, M., Gallego-Elvira, B., Garrigues, S., Mira, M., Marloie, O., and Boulet, G.: EVASPA, a tool for mapping evapotranspiration from space, ESA Living Planet Symposium, Prague, 9–13 May 2016, https://hal.inrae.fr/hal-03590489, 2016.

Olioso, A., Carriere, S., Allies, A., Sobrino, J. A., Skoković, D., Demarty, J., Boulet, G., Buis, S., and Weiss, M.: Uncertainty in evapotranspiration mapping from thermal infrared remote sensing data with EVASPA, Trishna Days, oral presentation, 2022.

Olioso, A., Carrière, S., Allies, A., Sobrino, J. A., Skoković, D., Demarty, J., Boulet, G., Buis, S., and Weiss, M.: Uncertainty in evapotranspiration mapping from thermal infrared remote sensing data with EVASPA: sensitivity to revisit time and orbital configuration, ESA ESRIN workshop / TRISHNA science meeting, Frascati, 2023.

Olioso, A., Chauki, H., Courault, D., and Wigneron, J.-P.: Estimation of evapotranspiration and energy fluxes using thermal infrared observations: a review of models and applications, Remote Sens. Environ., 140, 95–108, https://doi.org/10.1016/j.rse.2013.08.041, 2013.

Olioso, A., Inoue, Y., Ortega-Farías, S., and Wigneron, J.-P.: Advances in thermal infrared remote sensing for evapotranspiration estimation over heterogeneous surfaces, Remote Sens., 12, 1993, https://doi.org/10.3390/rs12121993, 2020.

Ollivier, C., Olioso, A., Carrière, S. D., Charlier, J.-B., Davi, H., Martin St-Paul, N. K., Weiss, M., Simioni, G., Marloie, O., Mazzilli, N., Chalikakis, K., Emblanch, C., Combemale, D., and Chanzy, A.: An evapotranspiration model driven by remote sensing data for assessing groundwater resource in karst watershed, Science of the Total Environment, 781, 146706, https://doi.org/10.1016/j.scitotenv.2021.146706, 2021.

Oltra-Carrió, R., Cubero-Castan, M., Briottet, X., and Sobrino, J. A.: Analysis of the performance of the TES algorithm over urban areas, IEEE Trans. Geosci. Remote Sens., 52, 6989–6998, https://doi.org/10.1109/TGRS.2014.2306441, 2014.

https://doi.org/10.5194/egusphere-2026-4492
Preprint. Discussion started: 31 July 2026

Perez, M. R., Araújo, R. G., Wiegmann, S., Torrecilla, E., Bardají, R., Röttgers, R., Bracher, A., and Piera, J.: Towards a cost-effective operational monitoring system for complex waters, PLoS ONE, https://doi.org/10.1371/journal.pone.0170706, 2017.

Pérez-Planells, L., Niclòs, R., Puchades, J., Coll, C., and Göttsche, F.-M.: Validation of Sentinel-3 SLSTR Land Surface Temperature Retrieved by the Operational Product and Comparison with Explicitly Emissivity-Dependent Algorithms, Remote Sensing, 13, 2228, https://doi.org/10.3390/rs13112228, 2021.

Picard, G., and Libois, Q.: Simulation of snow albedo and solar irradiance profile with the two-stream radiative transfer in snow (TARTES) v2.0 model, The Cryosphere, 16, 3861–3866, https://doi.org/10.5194/egusphere-2024-1176, 2024.

Pinel, N., Bourlier, C., and Sergievskaya, I.: Thermal IR emissivity of oil films on sea surfaces at moderate winds, OCEANS 2013 MTS/IEEE, https://doi.org/10.1109/OCEANS-Bergen.2013.6608011, 2013.

Pinty, B., et al.: Surface albedo retrieval from multiple-angle satellite data: application to POLDER, J. Geophys. Res. Atmos., 105, 18025–18041, 2000.

Prata, A. J.: Observations of volcanic ash clouds using AVHRR-2 radiances, Int. J. Remote Sens., 10, 751–761, 1989.

Prata, A. J.: Satellite detection of volcanic ash clouds and the hazards to aviation, Adv. Space Res., 43, 129–141, 2009.

Qin, W. and Goel, N. S.: An evaluation of hotspot models for vegetation canopies, Remote Sens. Rev., 13, 121–159, 1995.

Quattrochi, D. A., Estes, M. G., Crosson, W. L., and Khan, M. N.: The Atlanta urban heat island mitigation and air quality modeling project, AAG Meeting, Chicago, USA, 2006.

Ramsey, M. S., and Harris, A. J. L.: Volcanology 2020: how will thermal remote sensing of volcanic surface activity evolve over the next decade?, J. Volcanol. Geotherm. Res., 249, 217–233, 2013.

Ramsey, M. S., Harris, A. J. L., and Watson, I. M.: Volcanology 2030: will an orbital volcano observatory finally become a reality?, Bull. Volcanol., 84, 6, https://doi.org/10.1007/s00445-021-01501-z, 2022.

Rastogi, G., and Ajai: Energy balance modeling for ablation estimation of Gangotri Glacier, Journal of Geomatics, 7, 2013.

Rathore, B. P., Kulkarni, A. V., and Sherasia, N. K.: Understanding future changes in snow and glacier melt runoff due to global warming, Current Science, 97, 1077–1081, 2009.

Rathore, B. P., Singh, S. K., Bahuguna, I. M., Brahmbhatt, R. M., Rajawat, A. S., Thapliyal, A., Panwar, A., and Ajai: Spatio-temporal variability of snow cover in Himalayan sub-basins, Current Science, 108, 1375–1380, 2015.

Realmuto, V. J., Abrams, M. J., Buongiorno, M. F., and Pieri, D. C.: Use of multispectral thermal infrared image data to estimate sulfur dioxide flux from volcanoes, J. Geophys. Res., 99, 484–488, 1994.

Reinart, A., and Reynolds, M.: Mapping surface temperature in large lakes with MODIS data, Remote Sens. Environ., 112, 603–611, https://doi.org/10.1016/j.rse.2007.05.015, 2008.

Ren, H., Liu, R., Yan, G., Mu, X., Li, Z.-L., Nerry, F., and Liu, Q.: Angular normalization of land surface temperature and emissivity using multiangular middle and thermal infrared data, IEEE Trans. Geosci. Remote Sens., 52, 4913–4931, https://doi.org/10.1109/tgrs.2013.2285924, 2014.

Roberts, D. A., Quattrochi, D. A., Hulley, G. C., Hook, S. J., and Green, R. O.: Synergies between VSWIR and TIR data for the urban environment: evaluation for the HyspIRI mission, Remote Sens. Environ., 117, 83–101, https:/doi.org/10.1016/j.rse.2011.07.021, 2012.

Rogalski, A.: Infrared Detectors, 2nd ed., CRC Press, Boca Raton, 2011.

Roujean, J.-L., León-Tavares, J., Smets, B., Claes, P., Camacho de Coca, F., and Sánchez-Zapero, J.: Surface albedo and TOC-R 300 m products from PROBA-V instrument in the framework of Copernicus Global Land Service, Remote Sens. Environ., 215, 57–73, 2018.

https://doi.org/10.5194/egusphere-2026-4492
Preprint. Discussion started: 31 July 2026

Roujean, J.-L., Leroy, M., and Deschamps, P.-Y.: A bidirectional reflectance model of the Earth's surface for the correction of remote sensing data, J. Geophys. Res., 97, 20455, https://doi.org/10.1029/92jd01411, 1992.

Roujean, J.-L.: A parametric hot spot model for optical remote sensing applications, Remote Sens. Environ., 71, 197–206, https://doi.org/10.1016/s0034-4257(99)00080-2, 2000.

Roupioz, L., Nerry, F., and Colin, J.: Correction for the Impact of the Surface Characteristics on the Estimation of the Effective Emissivity at Fine Resolution in Urban Areas, Remote Sens., 10, 746, https://doi.org/10.3390/rs10050746, 2018.

Saraf, A. K., Choudhury, S., Rawat, V., Banerjee, P., Dasgupta, S., and Das, J. D.: Detecting earthquake precursors: a thermal remote sensing approach, Geospatial World, 2016.

Saunders, R., Matricardi, M., and Brunel, P.: A fast radiative transfer model for assimilation of satellite radiance observations – RTTOV-5, ECMWF Technical Report, 1999.

Schuurmans, J. M., Troch, P. A. A., Veldhuizen, A. A., Bastiaanssen, W. G. M., and Bierkens, M. F. P.: Assimilation of remotely sensed latent heat flux in a distributed hydrological model, Adv. Water Resour., 26, 151–159, https://doi.org/10.1016/S0309-1708(02)00089-1, 2003.

Seguin, B., Becker, F., Phulpin, T., Gu, X. F., and Guyot, G.: IRSUTE: a minisatellite project for land surface heat flux estimation from field to regional scale, Remote Sensing of Environment, 68, 357–369, https://hal.inrae.fr/hal-02579212, 1999.

Semmens, K. A., Anderson, M. C., Kustas, W. P., et al.: Monitoring daily evapotranspiration over two California vineyards using Landsat 8 and the thermal sharpening model, Remote Sens. Environ., 185, 13–28, https://doi.org/10.1016/j.rse.2015.10.025, 2016.

Shih, W.-C., and Andrews, A. B.: Infrared contrast of crude oil-covered water surfaces, Opt. Lett., 33, 3019–3021, https://doi.org/10.1364/ol.33.003019, 2008.

Singh, P., and Singh, V. P.: Snow and Glacier Hydrology, Kluwer Academic Publishers, 2001.

Singh, S. K., Rathore, B. P., Bahuguna, I. M., and Ajai: Snow cover variability in the Himalayan–Tibetan region, International Journal of Climatology, 34, 446–452, 10.1002/joc.3697, 2014.

Smith, J. A.: LAI inversion using a backpropagation neural network trained with multiple scattering model, IEEE Trans. Geosci. Remote Sens., 31, 1102–1106, 1993.

Sobrino, J. A., and Jiménez-Muñoz, J. C.: Minimum configuration of thermal infrared bands for land surface temperature and emissivity estimation in the context of potential future missions, Remote Sens. Environ., 148, 158–167, 2014.

Sobrino, J. A., Bianchi, R., Paganini, M., et al.: Final Report of the Dual-use European Security IR Experiment 2008 (DESIREX 2008), ESA Contract No. 21717/08/I-LG, 2009.

Sobrino, J. A., Del Frate, F., Drusch, M., Jiménez-Muñoz, J. C., Manunta, P., and Regan, A.: Review of Thermal Infrared Applications and Requirements for Future High-Resolution Sensors, IEEE Transactions on Geoscience and Remote Sensing, 54, 2963–2972, https://doi.org/10.1109/TGRS.2015.2509179, 2016.

Sobrino, J. A., Jiménez-Muñoz, J. C., Sòria, G., Ruescas, A. B., Danne, O., Brockmann, C., Ghent, D., Remedios, J., North, P., Merchant, C., Berger, M., Mathieu, P. P., and Göttsche, F.-M.: Synergistic use of MERIS and AATSR as a proxy for estimating land surface temperature from Sentinel-3 data, Remote Sens. Environ., 179, 149–161, https://doi.org/10.1016/j.rse.2016.03.035, 2016.

Sobrino, J. A., Oltra-Carrió, R., Sòria, G., Bianchi, R., and Paganini, M.: Impact of spatial resolution and satellite overpass time on evaluation of surface urban heat island effects, Remote Sens. Environ., 117, 50–56, 10.1016/j.rse.2011.04.042, 2012.

https://doi.org/10.5194/egusphere-2026-4492
Preprint. Discussion started: 31 July 2026

Sobrino, J., Lagouarde, J., Boulet, G., Briottet, X., Cherchali, S., Coudert, B., Dadou, I., Dedieu, G., Gillespie, A., Hagolle, O., et al.: Overview of the Thermal Infrared Explorer (TIREX) mission, Proc. Abstract Book 3rd Recent Adv. Quantitative Remote Sens., 213–214, 2010.

Stathopoulou, M., and Cartalis, C.: Downscaling AVHRR land surface temperatures for improved surface urban heat island intensity estimation, Remote Sens. Environ., 113, 2592–2605, https://doi.org/10.1016/j.rse.2009.07.017, 2009.

Stavros, E. N., Chrone, J., Cawse-Nicholson, K., Freeman, A., Glenn, N. F., Guild, L., et al.: Designing an observing system to study the Surface Biology and Geology (SBG) of the Earth in the 2020s, Journal of Geophysical Research: Biogeosciences, 128, e2021JG006471, https://doi.org/10.1029/2021JG006471, 2023.

Steinmetz, F., Deschamps, P.-Y., and Ramon, D.: Atmospheric correction in presence of sun glint: application to MERIS, Opt. Express, 19, 9783–9800, https://doi.org/10.1364/OE.19.009783, 2011.

Strahler, A. H., Muller, J.-P., et al.: MODIS BRDF/Albedo Product: Algorithm Theoretical Basis Document, version 5.0, 1999.

Su, L., Li, X., Friedl, M., Strahler, A., and Gu, X.: Kernel-driven model of effective directional emissivity for non-isothermal surfaces, Prog. Nat. Sci., 12, 603–607, 2002.

Su, Z.: The Surface Energy Balance System (SEBS) for estimation of turbulent heat fluxes, Hydrol. Earth Syst. Sci., 6, 85–100, https://doi.org/10.5194/hess-6-85-2002, 2002.

Tarantino, E.: Monitoring spatial and temporal distribution of Sea Surface Temperature with TIR sensor data, Italian Journal of Remote Sensing / Rivista Italiana di Telerilevamento, 44, 2012.

Thaïs Keravec-Balbot, Auline Rodler, Laure Roupioz, Marjorie Musy, Teddy Gresse, Xavier Briottet: Identification of urban thermal properties by combining urban microclimate modeling and thermal infrared satellite data, Sustainable Cities and Society, 118, 105995, ISSN 2210-6707, https://doi.org/10.1016/j.scs.2024.105995, 2025.

Thomas, A., Byrne, D., and Weatherbee, R.: Coastal sea surface temperature variability from Landsat infrared data, Remote Sensing of Environment, 81, 262–272, 2002.

Thuillier, G., et al.: Solar irradiance spectrum at solar minimum, Sol. Phys., 214, 1–22, 2003.

Trinh, R. C., Fichot, C. G., Gierach, M. M., Holt, B., Malakar, N. K., Hulley, G., and Smith, J.: Application of Landsat 8 for monitoring impacts of wastewater discharge on coastal water quality, Frontiers in Marine Science, 4, 329, 2017.

Tronin, A. A.: Satellite remote sensing in seismology: a review, Remote Sens., 2, 124–150, https://doi.org/10.3390/rs2010124, 2010.

Van der Kwast, J., Timmermans, J., Gieske, A., Su, Z., Olioso, A., Jia, L., Elbers, J., Karssenberg, D., and de Jong, S.: Evaluation of the SEBS model using ASTER imagery and flux measurements, Hydrol. Earth Syst. Sci., 13, 1337–1347, https://doi.org/10.5194/hess-13-1337-2009, 2009.

Vidal, T. H., Gamet, P., Olioso, A., and Jacob, F.: Optimizing TRISHNA TIR channels configuration for improved land surface temperature and emissivity measurements, Remote Sens. Environ., 272, 112939, 2022.

Vidal, T. H., Jacob, F., Olioso, A., and Gamet, P.: Optimization of instrumental spectral configurations for the split-window method in the context of the TRISHNA mission, IEEE Trans. Geosci. Remote Sens., 2021.

Vinnikov, K. Y., Yu, Y., Goldberg, M. D., Tarpley, D., Romanov, P., Laszlo, I., and Chen, M.: Angular anisotropy of satellite observations of land surface temperature, Geophys. Res. Lett., 39, https://doi.org/10.1029/2012gl054059, 2012.

Voogt, J. A., and Oke, T. R.: Thermal remote sensing of urban climates, Remote Sensing of Environment, 86, 370–384, https://doi.org/10.1016/S0034-4257(03)00079-8, 2003.

Walton, C. C., Pichel, W. G., Sapper, J. F., and May, D. A.: The development and operational application of nonlinear algorithms for the measurement of sea surface temperatures with the NOAA polar-orbiting environmental satellites, J. Geophys. Res. Oceans, 103, 27999–28012, https://doi.org/10.1029/98JC02311, 1998.

https://doi.org/10.5194/egusphere-2026-4492
Preprint. Discussion started: 31 July 2026

Wang, F., Meng, H., Xie, R., Wang, K., Ming, B., Hou, P., Xue, J., and Li, S.: Optimizing deficit irrigation and regulated deficit irrigation methods increases water productivity in maize, Agricultural Water Management, 280, 108205, https://doi.org/10.1016/j.agwat.2023.108205, 2023.

Wanner, W., Li, X., and Strahler, A. H.: On the derivation of kernels for kernel-driven models of bidirectional reflectance, J. Geophys. Res., 100, 21077–21089, https://doi.org/10.1029/95jd02371, 1995.

Watson, I. M., Realmuto, V. J., and Rose, W. I.: Thermal remote sensing of volcanic plumes and gas emissions, J. Volcanol. Geotherm. Res., 135, 75–89, https://doi.org/10.1016/j.jvolgeores.2003.12.007, 2004.

Weiss, M. and Baret, F.: S2ToolBox Level 2 Products: LAI, FAPAR, FCOVER, INRA, Avignon, France, 2016.

Weiss, M., Baret, F., Leroy, M., Hautecoeur, O., Bacour, C., Prévot, L., and Bruguier, N.: Validation of neural net techniques to estimate canopy biophysical variables from remote sensing data, Agronomie, 22, 547–553, 2002.

Weng, Q.: Thermal infrared remote sensing for urban climate and environmental studies: methods, applications, and trends, ISPRS J. Photogramm. Remote Sens., 64, 335–344, 2009.

Wooster, M. J., and Rothery, D. A.: Review of volcano surveillance applications using the ATSR instrument series, in: Advances in Environmental Monitoring and Modelling, 2000.

Yang, Y., Li, X., Liu, L., Chen, Y., and Huang, C.: A new downscaling method for thermal infrared remote sensing data based on a multi-sensor fusion approach, Remote Sens. Environ., 190, 14–28, 2017.

Yu, L., Zhao, X., Gao, X., and Siddique, K. H. M.: Improving/maintaining water-use efficiency and yield of wheat by deficit irrigation: A global meta-analysis, Agricultural Water Management, 228, 105906, https://doi.org/10.1016/j.agwat.2019.105906, 2020.

Zhou, Y., and Shepherd, J. M.: Atlanta's urban heat island under extreme heat conditions and potential mitigation strategies, Nat. Hazards, 52, 639–668, https://doi.org/10.1007/s11069-009-9406-z, 2010.